A PDMP model of the epithelial cell turn-over in the intestinal crypt including microbiota-derived regulations

Léo Darrigade, Marie Haghebaert, Claire Cherbuy, Simon Labarthe, Béatrice Laroche

Journal of Mathematical Biology manuscript No.
(will be inserted by the editor)

A PDMP model of the epithelial cell turn-over in the intestinal crypt including microbiota-derived regulations.

Léo Darrigade · Marie Haghebaert · Claire Cherbuy · Simon Labarthe · Beatrice Laroche

Received: date / Accepted: date

Abstract Human health and physiology is strongly influenced by interactions between human cells and intestinal microbiota in the gut. In mammals, the host-microbiota crosstalk is mainly mediated by regulations at the intestinal crypt level: the epithelial cell turnover in the crypts is directly influenced by metabolites produced by the microbiota. Conversely, the colonocytes maintain hypoxia in the gut, favorable to anaerobic bacteria which dominate the gut microbiota. We constructed an individual-based model of epithelial cells interacting with the microbiota-derived chemicals diffusing in the crypt lumen. This model is formalized as a piecewise deterministic Markov process (PDMP). It accounts for local interactions due to cell contact (among which are mechanical interactions), for cell proliferation, differentiation and extrusion which are regulated spatially or by chemicals concentrations. It also includes chemicals diffusing and reacting with cells. A deterministic approximated model is also introduced

L.Darrigade
Université Paris-Saclay, INRAE, MaIAGE, 78350, Jouy-en-Josas, France
E-mail: leo.darrigade@inria.fr
orcid : 0000-0002-2367-3414

M.Haghebaert
Université Paris-Saclay, INRAE, MaIAGE, 78350, Jouy-en-Josas, France
E-mail: marie.haghebaert@inrae.fr

C.Cherbuy
Université Paris-Saclay, INRAE, Micalis, 78350, Jouy-en-Josas, France
E-mail: claire.cherbuy@inrae.fr

S.Labarthe
Université Paris-Saclay, INRAE, MaIAGE, 78350, Jouy-en-Josas, France
Univ. Bordeaux, INRAE, BIOGECO, F-33610 Cestas, France
Inria, INRAE, Pléiade, 33400, Talence, France E-mail: simon.labarthe@inrae.fr
orcid: 0000-0002-5463-7256

B.Laroche
Université Paris-Saclay, INRAE, MaIAGE, 78350, Jouy-en-Josas, France
Université Paris-Saclay, Inria, Inria Saclay-Île-de-France, 91120, Palaiseau, France
E-mail: beatrice.laroche@inrae.fr
orcid : 0000-0001-7821-332X

for a large population of small cells, expressed as a system of porous media type equations. Both models are extensively studied through numerical exploration. Their biological relevance is thoroughly assessed by recovering bio-markers of an healthy crypt, such as cell population distribution along the crypt or population turn-over rates. Simulation results from the deterministic model are compared to the PMDP model and we take advantage of its lower computational cost to perform a sensitivity analysis by Morris method.

Keywords Piecewise Deterministic Markov Processes · Porous Media Equation · Crypt model · Host-microbiota interactions

1 Introduction

1.1 Colonic crypts: structure, regulations and interactions with the microbiota

The mammalian colon harbours a complex microbial community called the colonic microbiota. This microbiota is in constant and reciprocal interactions with its host and plays a key role in its nutrition and immunity. At the forefront of these interactions is the intestinal epithelium. It is a monolayer of cells lining the inside of the gastrointestinal wall, wrapped with a mucus layer in direct contact with the gut content. The intestinal epithelium is very densely folded and its smallest fold is called the intestinal crypt. The intestinal crypt is also the simplest unit of the host-microbiota crosstalk. It is an intensively studied biological system from various standpoints: stem cell biology [8,59], cell differentiation [66,69], biophysic [62,61,34] or interactions with the microbiota [68,48].

In the colon, a crypt is roughly shaped as a test tube of size 200×50 μm and contains hundreds of cells [49,65]. The colonic crypt is organised in three zones along its main axis [8], as shown in the Fig. 1. The bottom of the crypt, the farthest zone from the microbiota, is the stem cell niche. In this specific microenvironment reside epithelial stem cells and deep crypt secretory (DCS) cells [59]. Stem cells produce all other types of epithelial cells through successive divisions and differentiation, while DCS cells are differentiated cells with a key role in maintaining a favourable environment for stem cells. Above the stem cell niche are found progenitor cells. Progenitors are still dividing but they have started their differentiation path. Finally, in the upper part of the crypt, transit-amplifying cells have terminally differentiated in mostly two types of cells: enterocytes and goblet cells. Enterocytes are involved in the uptake of nutrients and water from the gut lumen and goblet cells secrete a protective layer of mucus covering the epithelium.

A striking feature of the colonic crypt is cell migration. Epithelial cells are produced at the bottom of the crypt by division of stem cells and are removed from the epithelium by extrusion at the top of the crypt. Cells therefore migrate from the bottom to the top of the crypt and differentiate along the way.

The functioning of the crypt relies on numerous and complex regulations. Of interest are regulations relying on contacts between neighbouring cells and regulations by molecules whose concentrations change along the crypt main axis. Other noteworthy examples of such regulation in the crypt are the Notch pathway [57,59] and the

EPH/ephrin signaling [11]. For several transcription factors (Wnt, BMP or Hedgehog), the concentration is a gradient between the bottom and the top of the crypt [71]. These trancription factors play an important part in crypt organisation. For example, Wnt is secreted by pericryptic cells at the bottom of the crypt and is necessary to maintain the pool of stem cells [25].

Epithelial cells interact with the colonic microbiota in multiple ways. A major interaction is the regulation of colon hypoxia, i.e. the depletion of oxygen in gut lumen, regulated by microbe-derived butyrate. Butyrate is a short-chain fatty acid produced at homeostasis by bacteria of the colonic microbiota by anaerobic fermentation of food fibers [38]. Dioxygen diffuses to the crypt from nearby blood vessels. At the bottom of the crypt, dividing host cells relie on anaerobic glycolysis (oxygen-free conversion of glucose to lactate) for their energy production, and consume little oxygen [26,2]. At the top of the crypt, differentiated epithelial cells consume butyrate and dioxygen through β-oxydation coupled to respiration to produce energy [38,33]. Therefore, the metabolic activity of differentiated epithelial cells renders the colonic epithelium hypoxic [38]. Little oxygen diffuses from the gastrointestinal wall to the colonic lumen which helps to maintain anaerobiosis in the colonic lumen. This is very important as some beneficial microbial species are obligate anaerobes whereas pathogens (*Salmonella enterica, Citrobacter rodentium*) or dysbiotic bacteria of the phylum Proteobacteria can utilize oxygen for their growth [38,16]. Conversely, if microbe-derived butyrate drops off, coloncytes switch their metabolism to anaerobic glycolysis, leading to oxygen release in the lumen which initiates a vicious circle harmful to butyrate producers and beneficial to dysbiotic bacteria. The idea is that the host keeps the colonic microbiota "on a leash" by controling the disponiblity of oxygen (and other electron acceptors) in the colonic lumen.

Butyrate also affects cellular processes beyond metabolism [41]. For example, butyrate has been reported to change the activity of important regulators of epithelial cell activity such as the nuclear receptor PPAR-γ [3], the heat shock protein Hsp25 [1] or the cell-cycle regulator Foxo3 [32]. Due to these interactions, butyrate was shown to reduce the proliferation of stem and progenitor cells, even inducing their apoptosis at high concentration [32,1], and to impact the differenciation processes of epithelial cells [51]. The effect of butyrate on stem and progenitor cells activity is observed in vitro at luminal concentration of butyrate. Therefore, it is hypothesized that the consumption of butyrate by differenciated cells of the upper part of the crypt is sufficient to drop concentrations of butyrate at a low level in the stem cell niche [32]. However, the concentrations of butyrate or oxygen are hard to measure in vivo and are therefore most of the time missing of the picture. This can undermine our understanding as contradictory effects have been reported depending on butyrate concentration and experimental conditions [60,50,55]. Our model is a step to fill this gap.

1.2 Existing models and achievement

There is a rich literature of intestinal crypt models, see [27] and [4] for a very recent review and references therein. Most of the proposed models are stochastic individual-based models (IBM) at the scale of epithelial cells. There exists also macroscopic

models formulated in terms of cells density [29,28], notably coming from physics. The link between the microscopic scale of IBMs and the macroscopic scale of cell density models has rarely been explored [46], most probably due to the complexity of IBMs and the lack of mathematical formalism. These crypt models are all largely motivated by issues arising from oncology such as clonal dynamics and stem cells competition in the crypt [39,64,67] or morphogenesis [15,36,67]. Some other models describe microbiota dynamics and digestive activity at the colonic scale, with however a very poor description of the epithelium [47,35,20,43].

In this work, our objective is to account for interactions with the microbiota in a healthy crypt model. To our knowledge, this is a new step in the modelling of intestinal crypts. In comparison with previous literature, we simplify crypt geometry and physical interactions between cells while retaining their essential features. Indeed these elements are not as important for understanding interactions with the microbiota as they are for other issues explored by crypt models, such as cell proliferation during oncogenesis or cryptogenesis. Instead, we put the emphasis on regulation processes directly or indirectly involved in crypt-microbiota cross-talk (see Sect. 2).

We propose an original model formulated as a piecewise deterministic Markov process (PDMP), which provides a rigorous mathematical framework. Our model couples a punctual measure that represents epithelial cells with spatially-structured concentrations of chemicals that mediate interactions between the crypt and the microbiota. The epithelial cells experience stochastic events governing their fate, and between two such events they move according to ODEs describing the mechanical constraints exerted on them, while reaction-diffusion PDEs model the chemical concentrations dynamics. Such a mixed ODE-PDE framework for a PDMP was already proposed e. g. in [14] in other biological contexts and our work follows the same lines. This detailed mathematical setting allows in particular for the derivation of a deterministic limit of the PDMP, which is more suitable than the stochastic version for intensive simulation required for instance in sensitivity analysis. On the other hand, as outlined in [4], the PDMP model provides outputs directly comparable to biological data, and which are more difficult to access with the deterministic model such as migration speed.

The description of the model is done in Sect. 2, and its deterministic limit is formally derived in Sect. 3. In Sect. 4, we propose a stepwise validation of the IBM model by decomposing it in elementary mechanisms that are studied sequentially and assessed by comparison with experimental values. Next, the global model is used to study the microbe-host interactions through butyrate and oxygen use. Finally, in Sect. 5, the deterministic limit of the PDMP model is implemented and explored by sensitivity analysis (Morris method).

2 A PDMP individual based-model of the crypt

We constructed an individual-based model of a colonic crypt at the scale of epithelial cells, interacting with butyrate or dioxygen which diffuse in cells environment. As shown in Fig. 1, this model accounts for 1) cell migration due to mechanical interactions between neighbouring cells, 2) cell division, extrusion and differentiation regu-

lated by chemicals concentrations, cell density and spatial position, and 3) diffusion and consumption of chemicals, leading to chemical gradients in the crypt. This model is a PDMP, or hybrid system: it mixes discrete stochastic events modeling sudden changes in the cell population such as differentiation, division or extrusion, and a deterministic flow modeling continuous population dynamics between this events, such as migration. With these elementary mechanisms, we want to reproduce biomarkers of an healthy crypt, such as proportion and spatial distribution of cell populations, migration speed of epithelial cells or crypt turn-over duration.

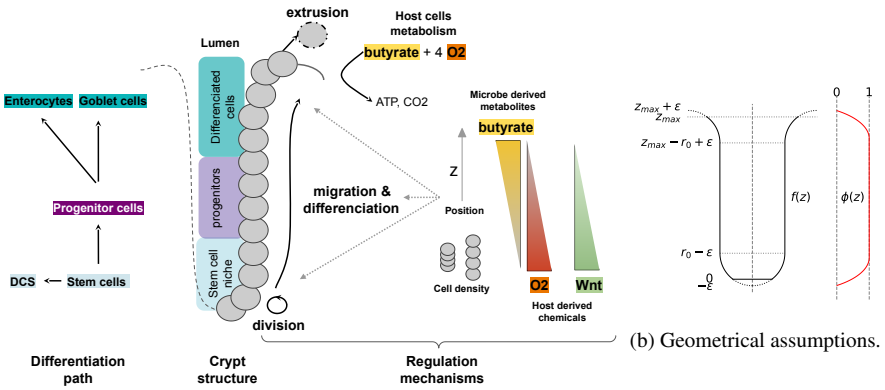

(a) Model components and mechanisms taken into account.

(b) Geometrical assumptions.

Fig. 1: **Summary of the model.** (a) **Model features and expected outcome.** First, the differentiation path between stem cells (sc), progenitor cells (pg) and differentiated cells (enterocytes (ent) and globet cells (gc)) is displayed in the leftmost part. Next, the spatial distribution of crypt cell populations at homeostasis (expected model outcome) is represented, from the stem cell niche at the bottom of the crypt, to the differentiated cells at the top. Finally, the regulation mechanisms (mechanical, metabolic and population dynamics mechanisms) driving the spatial structure in the model are listed, including the stochastic events (cell division, differentiation and extrusion), the cell migration, the cell density, the colonocyte metabolism and the metabolite gradients (butyrate, O_2 and Wnt)(b) **Crypt geometry.** We also indicate the geometrical assumptions underlying the definition of $f(z)$ including the profiles of the crypt domain and of the function ϕ defined in Eq. (4) modeling curvature effects in the mechanical model.

2.1 Model state description

We asssume that the crypt has cylinder symmetry around its vertical axis $[0, z_{max}]$ and is characterized by a truncated test-tube like shape (see figure 1b), with radius

$z \mapsto r(z)$ defined as

$$f(z) = \begin{cases} r_0\sqrt{\frac{z+\varepsilon}{r_0}\left(2-\frac{z+\varepsilon}{r_0}\right)} & \text{if } z \leq r_0 - \varepsilon \\ r_0 & \text{if } r_0 - \varepsilon < z < z_{max} - r_0 + \varepsilon \\ r_0\left(2-\sqrt{\frac{z_{max}-z+\varepsilon}{r_0}\left(2-\frac{z_{max}-z+\varepsilon}{r_0}\right)}\right) & \text{if } z \geq z_{max} - r_0 + \varepsilon \end{cases} \quad (1)$$

where we assume that r_0 is small compared to z_{max}, and ε is small compared to r_0.

For modeling interactions between epithelial cells and microbiota activity, the most relevant component of cell position in the crypt is the position along the crypt vertical axis. Therefore, we consider a spatial model of dimension one where each cell is characterized by its position $z \in [0, z_{max}]$ only, that is the projection of its actual spatial location on the crypt vertical axis. Consequently, several cells can be described by the same coordinate z, as several cells can be at the same height z in the 3D crypt.

A cell also has a type $l \in \mathscr{T}$, where $\mathscr{T}$ is a finite set comprising 5 different cell types: stem cell (*sc*), DCS cells (*dcs*), progenitor cells (*pc*), goblet cells (*gc*), enterocytes (*ent*).

Therefore, setting $\mathscr{X} = [0, z_{max}] \times \mathscr{T}$, a cell is characterized by the vector

$$x = (z, l) \in \mathscr{X}.$$

Let

$$\mathscr{M}_{P^+}(\mathscr{X}) = \left\{ \sum_{i=1}^{n} \delta_{x_i}(dx) : n \in \mathbb{N}^*; \forall i, x_i \in \mathscr{X} \right\}$$

be the set of positive finite punctual measures on $\mathscr{X}$, with $\sum_{i=1}^{0} \delta_{x_i}(dx)$ the null measure by convention. A population of n epithelial cells at time t is represented by:

$$\nu_t(dx) = \sum_{i=1}^{n} \delta_{x_i(t)}(dx) \quad \in \mathscr{M}_{P^+}(\mathscr{X})$$

where $x_i(t) = (z_i(t), l_i(t))$ is the vector of position and type of cell i at time t. For each cell type $l \in \mathscr{T}$, we denote by $\nu^l(dz) \in \mathscr{M}_{P^+}([0, z_{max}])$ the restriction of ν to a specific cell type (that is to say $\nu^l(Z) = \nu(Z \times \{l\})$ for any real borelian Z).

For a real-valued measurable function g on $\mathscr{X}$, the integral of g against ν will be

$$\langle \nu, g \rangle = \int_{\mathscr{X}} g(x)\nu(dx) = \sum_{i=1}^{n} g(x_i).$$

For a real-valued measurable function h on $\mathbb{R}$, we define the convolutions

$$\nu * h(z) = \sum_{l \in \mathscr{T}} \int_{[0, z_{max}]} h(z-y)\nu(dy, l) = \sum_{i=1}^{n} h(z - z_i)$$

and, for $l \in \mathscr{T}$,

$$\nu^l * h(z) = \int_{[0, z_{max}]} h(z-y)\nu^l(dy) = \sum_{i=1}^{n} h(z - z_i)\mathbb{1}_{\{l_i = l\}}.$$

Butyrate and dioxygen will be described by their respective concentrations $c_b(z,t)$ and $c_o(z,t)$ depending on space and time in suitable function spaces (see Sect. 2.2). In the following sections, we describe in details the behaviour of cells, as well as butyrate and dioxygen concentrations, by providing in Sect. 2.2 the deterministic flow of the PDMP and the stochastic events in Sect. 2.3.

2.2 Deterministic mechanisms of the PDMP model

The deterministic part of the PDMP models the cell movements and the reaction-diffusion of chemicals

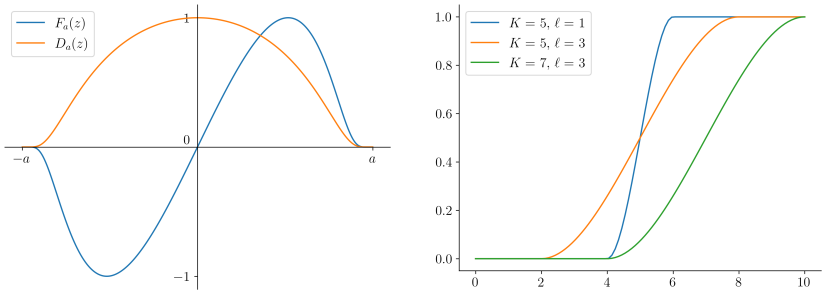

(a) Interaction functions F_a (with $k_a = 1$) and D_a (with $d_a = 1$). The function F_a describes repulsive forces, while D_a renders density dependant interactions.

(b) Regulation function $y \mapsto R(y,K,\ell)$ for various values of K and ℓ. The parameter K tunes the location of the transition and ℓ its width along the y axis.

Fig. 2: **Model function profiles.** Profiles of interaction kernels and regulation functions taken into account in the model

Mechanical interactions for cell migration. Cells in close proximity exert a repulsive force F_a on each other. In a population of n cells, we model the total force exerted on cell i as

$$\phi(z^i(t))\nu_t * F_a(z^i(t)) = \phi(z^i(t)) \sum_{j=1}^{n} F_a(z^i(t) - z^j(t)). \tag{2}$$

In this expression, we take into account the reduction of crypt geometry to the one dimensional z-axis in two ways.

First, in the real crypt, only neighbouring cells interact. This translates in our model to the fact that $F_a(z) := F(\frac{z}{a})$ where F is odd, compactly supported in $[-1,1]$, and a is the typical diameter of one cell. Moreover, in the original 3D conformation, cells that are sufficiently close to each other exert a force mostly normal to the z-axis. This translates in our 1D model into a decreasing amplitude as z goes to zero and

$F_a(0) = 0$. Therefore, we used the following expression for the force

$$F_a(z) = k_a \frac{\mathscr{F}_a(z)}{||\mathscr{F}_a||_\infty} \quad \text{where} \quad \mathscr{F}_a(z) = \begin{cases} \frac{z}{a} \exp\left(-\frac{\frac{|z|}{a}}{1-\frac{|z|}{a}}\right) & \text{if } |z| \leq a, \\ 0 \text{ otherwise.} \end{cases} \tag{3}$$

where k_a is a scaling parameter driving the maximal intensity of the force. F_a is plotted in Fig. 2a with $k_a = 1$.

Additionally, the function ϕ appearing in Eq.(2) aims to take into account the impact of curvature at the top and bottom of the crypt: in the curved zones, the interactions forces are exerted more radially, reducing their impact on the longitudinal cell kinematics. Consequently a phenomenological correction is applied to the total force, which takes the form of a linear function of the crypt radius $f(z)$, defined in (1), from 1 when $f(z) = r_0$ (i.e. no curvature) to 0 when $z = z_{max}$ or $z = 0$ (maximal curvature at both ends of the crypt). Namely, the correction is displayed in Fig. 1b and reads

$$\phi(z) := \begin{cases} \frac{\frac{f(z)}{r_0} - \frac{f(0)}{r_0}}{1-\frac{f(0)}{r_0}} & \text{if } z \leq r_0 - \varepsilon \\ 1 & \text{if } r_0 - \varepsilon < z < z_{max} - r_0 + \varepsilon \\ \frac{\frac{f(z_{max})}{r_0} - \frac{f(z)}{r_0}}{\frac{f(z_{max})}{r_0} - 1} & \text{if } z \geq z_{max} - r_0 + \varepsilon \end{cases} \tag{4}$$

Except for DCS cells (see below), the position of cell i evolves according to laws of classical mechanics taken in a non-inertial regime. This regime is known to correctly render the motion of individual cells in cell tissues where inertial terms can be neglected against other mechanisms [53]. The resulting equation of cell motion is

$$\frac{dz^i}{dt}(t) = \phi(z^i(t))\nu_t * F_a(z^i(t)) \quad \text{if } l^i \neq dcs \tag{5}$$

Note that, as $\phi(0) = \phi(z_{max}) = 0$, the speed of cells at the boundaries $z = 0$ and z_{max} is zero.

DCS cells are assumed to be "inactive", that is to say motionless ($\frac{dz^i}{dt}(t) = 0$), not dividing, not differentiating, not getting extruded. This is a simplification since it has been evidenced that the behaviour of DCS cells is quite complex and different from the rest of epithelial cells [59]. For example, they are thought to migrate downwards the crypt. Although inactive in the model, they exert mechanical forces on neighbouring cells and contribute to local cell density near the bottom of the crypt.

Reaction-diffusion of chemicals. As explained in section 1.1, butyrate is produced by the microbiota from fibers fermentation and O_2 is transported to the intestinal epithelium by the vascular system. Both molecules diffuse in the crypt and are consumed by goblet cells and enterocytes for energy production through β-oxidation. We summarize this metabolic pathway with the equation

$$1 \text{ butyrate} + 4\ O_2 \longrightarrow \text{ energy} + \text{ byproducts}.$$

Concentration of chemical $i \in \{butyrate,\ O_2\}$ evolves according to the reaction/diffusion equation on $]0, z_{max}[_a :=]-a/2, z_{max}+a/2[$

$$\partial_t c_i - \sigma_i \partial_{zz} c_i = -s_i \gamma_\beta^\infty \frac{c_o^4 c_b}{c_o^4 c_b + K_\beta^5} (\nu_t^{ent} + \nu_t^{gc}) * \psi_a(z) \tag{6}$$

where $\sigma_i > 0$ and s_i are respectively the diffusion constant and the stoechiometric coefficient of metabolite i. γ_β^∞ is the maximal reaction speed of β-oxydation, K_β is a positive constant, and $(\nu_t^{ent} + \nu_t^{gc}) * \psi_a(z)$ is the quantity of cell at z catalyzing the reaction. Indeed, introducing the function D_a

$$D_a(z) := d_a D(\frac{z}{a}), \quad \text{where} \quad D(z) := \begin{cases} \exp\left(-\frac{z^2}{1-z^2}\right) & \text{if } 0 \le |z| \le 1 \\ 0 & \text{otherwise,} \end{cases} \tag{7}$$

and d_a is a scaling parameter (see Fig. 2a with $d_a = 1$), we derive a normalized version of the density kernel D_a by writing

$$\psi_a(z) := \frac{D_{a/2}(z)}{\int_{-a/2}^{a/2} D_{a/2}(u)du}. \tag{8}$$

Then, for all $z \in [0, z_{max}]$, $\int_{]0,z_{max}[_a} \psi_a(z-y)dy = 1$. We see with this kernel definition that the extended domain $]0, z_{max}[_a$ has been introduced for compatibility reasons between the reaction-diffusion domain and the epithelial cell domain $]0, z_{max}[$.

This system of equations is supplemented with boundary conditions modeling the chemical fluxes at the crypt extremities. For butyrate:

$$\begin{cases} c_b = c_{b,lum} & \text{at } z = z_{max} + \frac{a}{2} \\ \partial_z c_b = 0 & \text{at } z = -\frac{a}{2} \end{cases} \tag{9}$$

and for oxygen:

$$\begin{cases} \partial_z c_o = 0 & \text{at } z = z_{max} + \frac{a}{2} \\ c_o = c_{o,bot} & \text{at } z = -\frac{a}{2} \end{cases} \tag{10}$$

Constant parameters $c_{i,lum}, c_{i,bot}$ represent the chemical concentrations in the gut lumen or at the bottom of the crypt, respectively reflecting microbial or host physiogy, and will be chosen depending on the biological context we want to model.

Furthermore initial conditions are defined : $c_b(0,z) = c_{b0}(z)$ and $c_o(0,z) = c_{o0}(z)$, for smooth c_{b0} and c_{o0} functions.

Deterministic flow. With classical arguments of system dynamics and PDE analysis (see Annex B), we can check for global existence of solution to the system (5-6), and define the associated deterministic flow for all $t > 0$.

$$\begin{gathered} A_t : H^1(]0, z_{max}[_a)^2 \times \mathscr{M}_{P^+}(\mathscr{X}) \longrightarrow H^1(]0, z_{max}[_a)^2 \times \mathscr{M}_{P^+}(\mathscr{X}) \\ (c, \nu) \longrightarrow A_t(c, \nu) \end{gathered}$$

where

$$A_t(c,\nu) = \left(A_t^0(c,\nu), \tilde{A}_t(c,\nu)\right) \quad \text{with} \quad \tilde{A}_t(c,\nu) := \sum_{i=1}^{\langle \nu,1\rangle} \delta_{(A_t^i(c,\nu),l^i)}.$$

$A_t(c,\nu)$ is the vector of solutions of the system (5-6) at time t for initial conditions (c,ν), with $A_t^0(c,\nu)$ the solutions (c_b,c_o) of Eq. (6) and $A_t^i(c,\nu)$, for $1 \leq i \leq \langle \nu,1\rangle$, the solution of Eq.(5). Note that $\langle \nu,1\rangle$ is the integral of the punctual measure ν against the function 1 and gives the number n of cells in the population ν. This number is constant under the deterministic flow.

By a direct application of the fundamental theorem of integration, we have the following equalities, holding for $f \in \mathscr{C}^1(\mathbb{R}^+ \times [0,z_{max}],\mathbb{R})$, $s,t \in \mathbb{R}^+$ and $1 \leq i \leq n$,

$$\begin{aligned} & f_t(A_t^i(c,\nu)) - f_s(A_s^i(c,\nu)) \qquad (11)\\ &= \int_s^t \phi(A_u^i(c,\nu))\tilde{A}_u(c,\nu) * F_a(A_u^i(c,\nu))\nabla_z f_u(A_u^i(c,\nu)) + \partial_u f_u(A_u^i(\nu))\, du \end{aligned}$$

and

$$\begin{aligned} \langle \tilde{A}_t(c,\nu), f_t\rangle - \langle \tilde{A}_s(c,\nu), f_s\rangle = \int_s^t \langle \tilde{A}_u(c,\nu), \phi(\cdot)\tilde{A}_u(c,\nu) * F_a(\cdot)\nabla_z f_u(\cdot) \\ + \partial_u f_u(\cdot)\rangle\, du. \qquad (12) \end{aligned}$$

2.3 Stochastic modeling of cell fate

The PDMP takes into account seven possible event types in cell population dynamics, modeled as stochastic punctual events, or jumps. They are indexed by $k \in \mathscr{E}$ the finite set of event types. These events are the symmetric division of stem and progenitor cells, the death by extrusion of enterocytes and goblet cells and the differentiation of stem cells into progenitors, as well as the differentiation of progenitors into enterocytes and goblet cells (see Fig. 1a for an overview of the events). Their construction is described below.

Stochastic jumps during cell fate. Jump functions are defined for all type of cells. When at T the cell i undergoes a jump of type k, the population is modified as

$$\nu_T = \nu_{T^-} + \mu_k(x^i(T^-))$$

where

$$\mu_k : \quad \mathscr{X} \to \mathscr{M}_P(\mathscr{X}), \qquad (13)$$

with $\mathscr{M}_P(\mathscr{X}) = \{\sum_{i=1}^n \pm\delta_{x_i}(dx) : n \in \mathbb{N}^*; \forall i, x_i \in \mathscr{X}\}$ the set of punctual finite measures on $\mathscr{X}$. More precisely,

- if k is a division, a new daughter cell is introduced at a distance $\lambda(z)$ above (resp. under) the mother cell in the lower (resp. upper) part of the crypt, leading to

$$\mu_k(z,l) = \delta_{(z+\lambda(z),l)}$$

with

$$\lambda(z) = \begin{cases} \frac{a}{2} & \text{if } z \leq z_{max}/2 - a, \\ \frac{-a}{2} & \text{if } z \geq z_{max}/2 + a, \\ \frac{a}{2} - a\frac{z-(z_{max}/2-a)}{2a} & \text{otherwise,} \end{cases}$$

so that $\forall z \in [0, z_{max}]$, $z + \lambda(z) \in [0, z_{max}]$,
- if k is an extrusion $\mu_k(x) = -\delta_x$,
- if k is a differenciation of a cell of type l into a type l_k then

$$\mu_k(z,l) = -\delta_{(z,l)} + \delta_{(z,l_k)}.$$

Jump rates. We model three biological regulations acting on events of cell fate. The first one depends on cell variables (position and cell type). The dependence on the position models the action of morphogenes, in particular Wnt, on the cell differenciation: we assume a fixed linearly decreasing gradient of Wnt in the crypt, so that the Wnt density can be modeled by the position $z \in]0, z_{max}[$ up to scaling parameters. The dependence on the cell type ensures that only the seven possible jump types occur, by setting the jump rate to zero when necessary.

The second one depends on the local cell density $\mathbf{d}$ defined by

$$\mathbf{d}(\nu_t, z) = d(z)\,(\nu_t * D_a)\,(z)$$

where D_a is defined in Eq.(7) and

$$d(z) = \frac{\int_{-a}^{a} D_a(u)\,du}{\int_{\max(-a,-z)}^{\min(a,z_{max}-z)} D_a(u)\,du}. \tag{14}$$

The function $d(z)$ is then a normalization coefficient insuring that the kernel D_a keeps the same integral along $[0, z_{max}]$, included near the boundaries where the integral can be cut off, in order to account for the 1D approximation.

The third regulation depends on the local concentration of butyrate $\mathbf{c_b}$ defined by

$$\mathbf{c_b}(z) = c_b * \psi_a(z)$$

where $\psi_a(z)$ is introduced in Eq. (8).

Then, the individual jump rate associated to each jump $k \in \mathscr{E}$ is defined as

$$q_k^{\infty} q_k(x, \mathbf{d}(\nu_t, z), \mathbf{c_b}(z)) \tag{15}$$

where q_k^{∞} is a positive constant equals to the maximal rate of jump and $0 \leq q_k(\cdot) \leq 1$.

To define the normalized jump rate q_k, we introduce a generic regulation function $R(y, K, l)$ for $y \geq 0$, $K > 0$, $\ell > 0$, that will model the dependence of q_k to the variable y ($y = z$ for space regulation i.e. Wnt regulation, $y = \mathbf{d}(\nu_t, z)$ for density regulation or $y = \mathbf{c_b}(z)$ for butyrate regulation) parametrized by jump and regulation dependant

parameters $K_k[j]$ and $\ell_k[j]$ where index k refers to the jump type and j to the regulation pathway (see equation (17) for an explicit example). Namely, we define the piecewise polynomial function $R(y,K,\ell)$ (plotted on Fig. 2b for several values of k_a and ℓ) by

$$R(y,K,\ell) := \begin{cases} 0 & \text{if } y \leq K-\ell, \\ -\frac{1}{4\ell^3}y^3 + \frac{3K}{4\ell^3}y^2 - \frac{3K^2-3\ell^2}{4\ell^3}y + \frac{K^3+2\ell^3-3K\ell^2}{4\ell^3} & \text{if } K-\ell \leq y \leq K+\ell, \\ 1 & \text{if } K+\ell \geq y. \end{cases} \tag{16}$$

Note that R connects continuously the values 0 and 1 for $K-\ell < z < K+\ell$ and has value $1/2$ in $y = K$. The normalized individual jump rate $q_k(x, \mathbf{d}(\nu_t, z), \mathbf{c_b}(z))$ associated to event k is a product over the regulations j of functions $R(\cdot, K_k[j], \ell_k[j])$ for an activation or $(1 - R(\cdot, K_k[j], \ell_k[j]))$ for an inhibition.

$$\begin{aligned} q_{div,sc}(z,l,\mathbf{d}(\nu_t,z),\mathbf{c_b}(z)) = \overbrace{\mathbb{1}_{\{l=sc\}}}^{\text{0 if not stem cell}} & \times \overbrace{(1-R(z,K_{div,sc}[z],\ell_{div,sc}[z]))}^{\text{regulation by Wnt}} \\ & \times \overbrace{(1-R(\mathbf{d}(\nu_t,z),K_{div,sc}[dens],\ell_{div,sc}[dens]))}^{\text{regulation by density}} \\ & \times \underbrace{(1-R(\mathbf{c_b}(z),K_{div,sc}[but],\ell_{div,sc}[but]))}_{\text{regulation by butyrate}}. \end{aligned} \tag{17}$$

The different biological regulations we used, based on the biological knowledge presented in Sect. 1.1, are summarized in Table 1 and detailed in Annex A.2. The parameter values q_k^∞, $K_k[j]$ and $\ell_k[j]$ can be found in Table 11. Note that each jump type is not necessarily regulated by all three regulation pathways (for example, the rate of extrusion does not depend on butyrate concentration). When a regulation pathway is neutral for a jump, the corresponding term is set to the constant value 1. Remember as well that, as we supposed a stable linearly decreasing spatial gradient of Wnt, an inhibitory effect of Wnt corresponds in our model to an activation by the position z. Finally, the choice of using a product of regulation functions $R(\cdot)$ (and $1-R(\cdot)$) instead of a sum corresponds to the biological hypothesis that the regulation pathways are not independent.

2.4 Numerical implementation of the PDMP

We implemented the model in `Python 3`. The code sources can be found at `https://forgemia.inra.fr/decrypt/pdmp-model`. To solve the PDMP, we use a standard Gillepsie algorithm with an acceptation-reject method for stochastic events. The deterministic flow is solved with an explicit Euler method for the cell movement, and with a semi-implicit Euler scheme with operator splitting to compute the reaction-diffusion equations on butyrate and oxygen. Cells are sorted in a `NumPy` array according to their position, allowing to compute interactions only between groups of neighbouring cells. `Numba` package is used for further code acceleration.

Jump type	Jump index (k)	Regulation pathway (j)		
		butyrate [*but*]	Wnt [z]	density [*dens*]
Stem cell division	div, sc	$-$	$-$	$-$
Progenitor division	div, pc	$\varnothing$	$-$	$-$
Stem cell to progenitor differentiation	sc, pc	$\varnothing$	$+$	$\varnothing$
Progenitor to globlet cell differentiation	pc, gc	$+$	$+$	$\varnothing$
Progenitor to enterocyte differentiation	pc, ent	$+$	$+$	$\varnothing$
Goblet cell extrusion	ex, gc	$\varnothing$	$+$	$+$
Enterocyte extrusion	ex, ent	$\varnothing$	$+$	$+$

Table 1: **Enumeration of stochastic jump types and their corresponding regulation.** For the jump k and a given regulation pathway j, a negative regulation ($-$) is represented by the term $(1-R(y,K_k[j],\ell_k[j]))$, a positive regulation ($+$) by the term $R(y,K_k[j],\ell_k[j])$ and a neutral regulation ($\varnothing$) by a constant value equal to 1, where $y=z$, $y=\mathbf{d}(\nu_t,z)$ or $y=\mathbf{c_b}(z)$ for respectively position, density or butyrate regulation. As we supposed a stable linearly decreasing spatial gradient of Wnt, a negative regulation by position z corresponds to the biological hypothesis of a positive regulation by Wnt. The values of $K_k[j]$ and $\ell_k[j]$ can be found in Table 11. Detailed formulations can be found in Annexe A.2.

3 Deterministic approximation of the PDMP.

To derive the deterministic approximation of the PDMP, we first set a functional framework in which the PDMP model is well-posed. Then, a formal approximation is derived in this setting.

3.1 Functional setting and well-posedness

With the definitions above, all the ingredients needed for the definition of a PDMP are now gathered (see e.g. [31]):

- the process state space $G=H^1(]0,z_{max}[_a)^2\times\mathscr{M}_{P^+}(\mathscr{X})$, which is a Polish space equipped with a distance defined as the product of the distance induced by the H^1 norm and the Prokhorov metric (see Proposition A.2.5.III [22] and Proposition A.5 [23]).
- a measurable and time-continuous deterministic flow A, also continuous respectively to its parameters. To prove the later, the only technical point is to show the continuity of the concentrations $A^0_t(c,\nu)$ with respect to ν and it can be deduce from Property 2.13, Chapter 4 of [23].
- a total jump intensity $q: G\to\mathbb{R}^+$, defined by

$$q(c,\nu)=\sum_{k\in\mathscr{E}}\sum_{i=1}^{\langle\nu,1\rangle}q_k^\infty q_k(x_i,\mathbf{d}(\nu_t,z_i),\mathbf{c_b}(z_i))=\langle\sum_{k\in\mathscr{E}}q_k^\infty q_k(.,\mathbf{d}(\nu_t,.),\mathbf{c_b}(.)),\nu\rangle$$

which only depends on the current process state, and is continuous in its arguments. Moreover, q is locally right-integrable in time along deterministic trajec-

tories, namely,

$$\int_t^{t+h} q(A_{s-t}(c,\nu))ds \leq h|\mathscr{E}| \max_k(q_k^\infty)\langle \nu, 1\rangle < +\infty$$

since the cell population size only changes during stochastic jumps and does not vary during deterministic trajectories.

– a Markov kernel r defined on G with

$$r(c,\nu) = \sum_{k\in\mathscr{E}} \sum_{i=1}^{\langle \nu,1\rangle} \frac{q_k^\infty q_k(x_i, \mathbf{d}(\nu_t, z_i), \mathbf{c_b}(z_i))}{q(c,\nu)} \delta_{(c,\nu+\mu_k(x^i))},$$

that only depends on the current state.

We have shown in Sect. 2.2 and Annex B that the determinist trajectory of the process between jumps is defined globally. The well-posedness of the PDMP will follow once we prove the stability of the PDMP ([31], theorem 3.2.1), that is to say that an almost surely finite number of jumps occurs during any finite time interval. This is done in the Annex C and in [23].

3.2 Deterministic limit of the PDMP

When the size of the cell population becomes large ($\langle \nu_N, 1\rangle \in O(N)$ with $N \to \infty$), the corresponding sequence of models with a rescaled cell population $(c_N, \nu_N/N)$ and rescaled parameters

$$F_a^N = \frac{F_a}{N},\ D_a^N = \frac{D_a}{N} \text{ and } \psi_a^N = \frac{\psi_a}{N}$$

converges in the space

$$C([0,T], H^1(]0, z_{max}[_a))^2 \times \mathscr{D}([0,T], \mathscr{M}_{F^+}(\mathscr{X})),$$

where $\mathscr{D}([0,T], \mathscr{M}_{F^+}(\mathscr{X}))$ is the space of *càdlag* functions from $[0,T]$ in the space $\mathscr{M}_{F^+}(\mathscr{X})$ of finite positive measures on $\mathscr{X}$, equipped with the Prokhorov metric. The convergence takes place in the sense of the weak topology, provided that $(c_{N0}, \nu_{N0}/N)$ converges weakly to (c_0, ξ_0) in $H^1(]0, z_{max}[_a)^2 \times \mathscr{M}_{F^+}(\mathscr{X})$. The limit (c, ξ) satisfies a *self-aggregation* equation

$$\begin{aligned}\langle \xi_t, f_t\rangle = \langle \xi_0, f_0\rangle &+ \int_0^t \langle \xi_s, \phi(\xi_s * F_a)\partial_z f_s + \partial_t f_s\rangle ds \\ &+ \sum_{k\in\mathscr{E}} \int_0^t \sum_{l\in\mathscr{T}} \int_{\mathscr{Z}} \langle \mu_k(z,l), f_s\rangle q_k^\infty q_k(z,l,\mathbf{d}(\xi_s,z), \mathbf{c_b}_s(z))\xi_s(dz,l)ds \quad (18)\end{aligned}$$

for all $f = (f^{(1)}, \cdots, f^{(|\mathscr{T}|)}) \in (\mathscr{C}^1(\mathbb{R}^+ \times [0, z_{max}], \mathbb{R}))^{|\mathscr{T}|}$, where

$$\langle \xi_t, f_t\rangle = \sum_{l\in\mathscr{T}} \int_0^{z_{max}} f^{(l)}(t,z)\xi_t^l(dz)$$

and ξ_t^l is the restriction of ξ_t to cells of type l.
Moreover, for $i \in \{butyrate, O_2\}$ we have

$$\partial_t c_i - \sigma_i \partial_{zz} c_i = -s_i \gamma_\beta^\infty \frac{c_o^4 c_b}{c_o^4 c_b + K_\beta^5} (\xi_t^{ent} + \xi_t^{gc}) * \psi_a(z)$$

with the same boundary conditions as in (9,10).

The proof of this result is technical and not provided here but can be found in Chapter 4 of [23]. This deterministic limit is however quite natural. Indeed, the partial differential operator $\int_0^t \langle \xi_s, \phi(\xi_s * F_a)\partial_z f_s + \partial_t f_s \rangle ds$ has the same form as the deterministic flow in (12) where $\tilde{A}_t(c,v)$ is replaced by its limit ξ_s. For the stochastic part of the model, this limit is a standard result for punctual jump processes (see e.g. Chapter 7 in [7]). The fact that this stochastic part is coupled to a PDE-based deterministic flow in a PDMP leads to specific technical issues that are rigorously dealt with in [23].

Let $Div = \{div, sc; div, pc\} \subset \mathscr{E}$ denotes the set of division events, $Ex = \{ex, gc; ex, ent\}$ denotes the set of extrusion events and $Dif = \{sc, pc; pc, gc; pc, ent\}$ denotes the set of differentiation events. If we assume that for all cellular type l, the restricted measures $\xi_t^l(dz)$ have a density denoted $\rho_l(z,t)$ on $[0, z_{max}]$, then (18) is a weak formulation of the system

$$\begin{aligned} \partial_t \rho_l + \partial_z \Big(\phi \rho_l (\rho * F_a)) \Big) &= \sum_{k \in \mathscr{E} \setminus Div} \eta_{k,l} q_k^\infty q_k(z, l, \mathbf{d}(\rho, z), \mathbf{c_b}(z)) \\ &+ \sum_{k \in Div} \eta_{k,l}(z - \lambda(z)) q_k^\infty q_k(z - \lambda(z), l, (d \times \rho * D_a)(z - \lambda(z)), \mathbf{c_b}(z - \lambda(z)) \end{aligned} \tag{19}$$

where $\rho = \sum_l \rho_l$ is the total local cell density and

$$\eta_{k,l} = \begin{cases} \rho_l & \text{if } k \in Div \\ -\rho_l & \text{if } k \in Ex \\ \rho_{l_k} & \text{if } k \in Dif \text{ and for a differentiation from type } l_k \text{ into type } l \\ -\rho_l & \text{if } k \in Dif \text{ and for a differentiation from type } l \end{cases} \tag{20}$$

We can go one step further, as suggested in [23], and derive a formal approximation of the model when the cell size a goes to zero.

We introduce the potential

$$W_a(z) = -\int_{-a}^{z} F_a(y) dy.$$

From the definition of F_a in (3), we see that $F_a(z) = \frac{k_a}{k_1} F_1(\frac{z}{a})$ and therefore $W_a(z) = a\frac{k_a}{k_1} W_1(\frac{z}{a})$. From the definition of D_a in (7), we see that $D_a(z) = \frac{d_a}{d_1} D_1(\frac{z}{a})$. We assume that

$$k_a = \frac{k_1}{a^2} \quad \text{and} \quad d_a = \frac{1}{a}.$$

If the densities in (19) are smooth and using the change of variables $\tilde{y} = y/a$ in the convolutive terms we have after some computation

$$\rho * F_a(z) = -\rho * W_a'(z) = -\int_{-a}^{a} \rho'(z-y) W_a(y) dy$$
$$= -a^2 \frac{k_a}{k_1} \int_{-1}^{1} W_1(\tilde{y}) \rho'(z-a\tilde{y}) d\tilde{y} = -\int_{-1}^{1} W_1(\tilde{y}) \rho'(z-a\tilde{y}) d\tilde{y}$$

and

$$\mathbf{d}(\rho, z) = d(z) (\rho * D_a)(z) = d(z) \int_{-1}^{1} \rho(z-a\tilde{y}) D_1(\tilde{y}) d\tilde{y}.$$

The function d converges pointwise towards 1 when $a \to 0$ on the open interval $]0, z_{max}[$. So

$$\rho * F_a(z) \underset{a\to 0}{\longrightarrow} -W \partial_z \rho(z), \qquad \mathbf{d}(\rho, z) \underset{a\to 0}{\longrightarrow} D\rho(z)$$

with $W = \int_{-1}^{1} \int_{-1}^{y} F_1(z) dz dy$ and $D = \int_{-1}^{1} D_1(z) dz$. Likewise,

$$\mathbf{c_b}(z) \underset{a\to 0}{\longrightarrow} c_b(z), \rho_l * \psi_a(z) \underset{a\to 0}{\longrightarrow} \rho_l(z) \text{ and } \lambda(z) \underset{a\to 0}{\longrightarrow} 0.$$

It follows that when a goes to zero, the self-aggregation equations for the densities have the following formal approximation for all l in $\mathscr{T}$

$$\partial_t \rho_l - W \partial_z (\phi(z) \rho_l \partial_z \rho) = \sum_k \varepsilon_{k,l} q_k^{\infty} q_k(z, l, D\rho, c_b), \tag{21}$$

These equations are complemented with the following mixed boundary conditions, chosen for their simplicity. They reflect the absence of cells at the bottom of the crypt but stem cells, and zero flux condition at the top.

$$\rho_l(0,t) = 0 \text{ if } l \neq sc, \quad \rho_{sc}(0,t) = \rho_{sc}^{bot},$$
$$\partial_z \rho_l(z_{max}, t) = 0.$$

The coupled reaction-diffusion equations are, for $i \in \{butyrate, O_2\}$,

$$\partial_t c_i - \sigma_i \partial_{zz} c_i = -s_i \gamma_{\beta}^{\infty} \frac{c_o^4 c_b}{c_o^4 c_b + K_{\beta}^5} \times (\rho_{ent} + \rho_{gc})$$

with the same boundary conditions as in (9,10).

Equation (21) is a porous media equation (PME) type. More precisely, the nonlinear diffusion term $W \partial_z (\phi(z) \rho_l \partial_z \rho)$ can be interpreted as a Darcy law for incompressible fluids in a porous media (according to which the advection speed is proportional to the local pressure gradient) where the pressure is proportional to the local total density of cells. Such equations have already been suggested to model densities of interacting cells [40,45,46]. The equations present a non linear cross-diffusion term coming from the presence of $\rho(z,t) = \sum_{l \in \mathscr{T}} \rho_l(z,t)$, the total cell density. The source terms are formally derived from the expressions given above for the self-aggregation equations. The spatial shift λ for introduction of daughter cells during cell division now vanishes in the deterministic limit, since the cell radius is assumed to be small. In other words, daughter cells are introduced at the same place as mother cells during division in the deterministic model.

3.3 Numerical implementation

The porous media type equations (21) are not trivial to solve, due to the non linear cross-diffusion terms, and requires adapted numerical tools. The kinetic diffusive explicit scheme described in [5] and used in [70] designed for nonlinear transport diffusion equations allowed us to obtain satisfactory simulations. Therefore, letting $\hat{\rho}_l = \sum_{k \neq l} \rho_k$ and $G(z) = \frac{1}{2} W \phi(z)$, we modified (21) to obtain the system of transport-diffusion equations with source terms

$$\partial_t \rho_l - \partial_z \left(W \phi \partial_z (\hat{\rho}_l) \rho_l + G' \rho_l^2 \right) - G \partial_{zz} \rho_l^2 = -G'' \rho_l^2 + \sum_k \eta_{k,l} q_k^\infty q_k(z, l, D \times \rho, c_b) \tag{22}$$

which is the model structure needed for the kinetic diffusive explicit scheme. The python code is available at `https://forgemia.inra.fr/decrypt/deterministic-model`.

The deterministic approximation is fastest to compute and allows us to perform more intensive numerical explorations than with the PDMP. On the other hand, the stochastic model is relevant to extract features directly comparable with biological observations, such as migration speed, cell fate tracking or renewal rates. In the sequel, we will first explore the PDMP model and show that it renders accurately the main features of an healthy crypt in term of population distribution and turn-over. Then, we will verify that the deterministic limit (21) provides an accurate approximation of the PDMP model for sufficiently small cells and we will carry out a systematic sensitivity analysis of the deterministic limit using the Elementary Effects method of Morris. This sensitivity analysis would not have been tractable with the original PDMP model due to an excessive computational load.

4 Numerical exploration of the PDMP model

We now show that simulations reproduce qualitatively the behaviour of a distal colonic mouse crypt. To understand the behaviour of our model, we did not start by simulating the full model presented in Sect. 2. We rather conducted a sequence of numerical experiments on submodels of increasing complexity, adding at each step new components from the full model. In 4.1, we explore the sole effect of cell-cell mechanical interactions. In 4.2, we reproduce the migration of epithelial cells by adding spatially regulated division and extrusion to the mechanical interactions. In 4.3, we explore the spatial distribution of cell populations by adding cell types and spatial regulation of differenciation. In 4.4, we add butyrate and oxygen diffusion and consumption by epithelial cells, and finally, in 4.5, we compute the whole model by adding butyrate regulation on cell fate.

4.1 Cell layers formation due to mechanical interactions

We begin our experiments with a population of identical cells subject only to mechanical interactions, with no stochastic events whatsoever. Parameters values are given in Table 7. Starting with a uniform cell distribution in the crypt, we observe that cells

rapidly gather into layers. This phenomenon is allowed by the specific shape of the interaction function F_a, as $F_a(0) = 0$. As expected, the spacing between layers is influenced by the cell diameter a which is the unique parameter of the interaction kernel (Fig. 3).

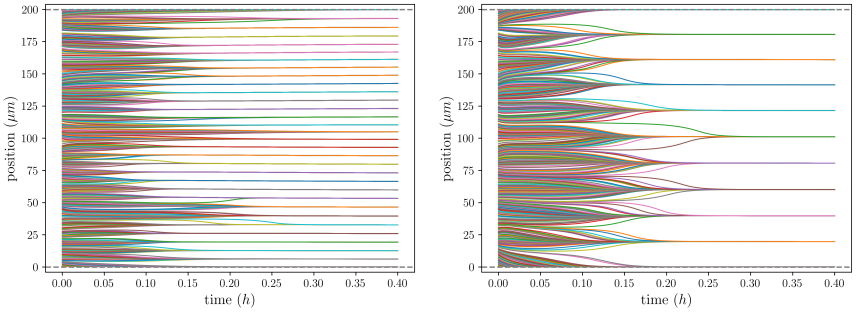

(a) Cell diameter $a = 10\ \mu m$. (b) Cell diameter $a = 30\ \mu m$.

Fig. 3: **Trajectory of cells due to repulsive mechanical interactions only.** Initial positions of 700 cells are drawn in a law $U(0, z_{max})$, with same initial condition for both simulations.

4.2 Migration effect

Migration of epithelial cells is a hallmark behaviour of the intestinal crypt. As explained in Sect. 1.1, epithelial cells are produced by division of undifferentiated cells in the bottom third of the crypt and migrate to the upper part of the crypt where they are extruded. We can reproduce this phenomenon by simply adding to the previous sub-model stochastic division and extrusion that are regulated spatially and by density.

We consider a population of identical cells, interacting mechanically through Eq. (5), which divide and are extruded with respective rates $q_{div}(\cdot)$ and $q_{ex}(\cdot)$:

$$q^{\infty}_{div} q_{div}(z, \nu * D_a(z)) = q^{\infty}_{div} \overbrace{R(z, K_{div}[z], \ell_{div}[z])}^{\text{regulation by position}} \times \overbrace{R(\nu * D_a(z), K_{div}[dens], \ell_{div}[dens])}^{\text{regulation by density}}, \tag{23}$$

$$q^{\infty}_{ex} q_{ex}(z, \nu * D_a(z)) = q^{\infty}_{ex} \underbrace{R(z, K_{ex}[z], \ell_{ex}[z])}_{\text{regulation by position}} \times \underbrace{(1 - R(\nu * D_a(z), K_{div}[dens], \ell_{div}[dens]))}_{\text{regulation by density}}. \tag{24}$$

Figure 4a shows the trajectory of cells in the crypt, during one realization of the PDMP. The initial positions of 700 cells are drawn from a spatial uniform distribution, as in Sect. 4.1, and parameter values are given in Table 8. With the addition of

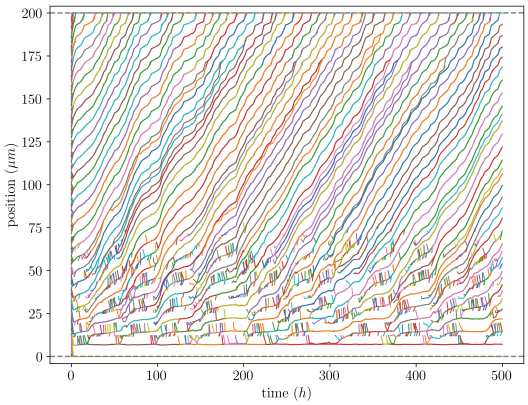

(a) Trajectory of cells

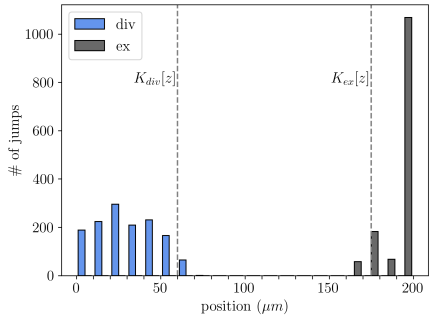

(b) Spatial repartition of jumps

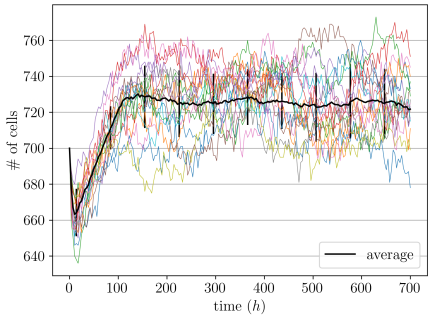

(c) Number of cells

Fig. 4: **Cell migration.** For an initial condition of 700 cells uniformly distributed along the crypt, we indicate the cells trajectories (a) and the spatial distribution of stochastic events (b) for one simulation, and the number of cells for 16 randomly selected simulations, as well as the mean and standard deviation for 50 repetitions of the PDMP (c). Division events are visible in (a) with comb-like patterns in the lower zone of the crypt corresponding to daughter cell that joins a close layer. As expected, division and extrusion are spatially segregated (b). A stationary number of cells is reached after about 200 hours, indicating an equilibrium between division and extrusion (c).

spatially regulated division and extrusion events, we see that cells migrate from the bottom to the top of the crypt. In the lower zone of the crypt ($z \leq 75\mu m$), cell division occurs. When a new cell is introduced at a distance $a/2$ of the mother cell, it rapidly joins a close cell layer as illustrated in the previous Sect. 4.1. This corresponds to the comb-like patterns in Fig. 4a. Figure 4b shows the number of division and extrusion events according to the position in the crypt, for the same realization as Fig. 4a. As in normal crypts, division occurs at the bottom of the crypt and extrusion at the top, fueling the migration phenomena. We finally display the time evolution of the

number of cells, and the mean over 50 realizations of the PDMP in Fig. 4c. We can observe that the total population reaches a stationary state of around 740 cells after about 200 hours, with little stochastic variations around this value. This stationary state indicates an equilibrium between division and extrusion.

Interesting biomarkers evaluated during experiments to quantify the crypt activity are the total cell population (TCP), the average migration speed (MS) and the individual division rate (DR). In our model, possible drivers of these quantities are the interaction intensity k_a, the extrusion rate q_{ex}^{∞} and the sensitivity to cell density of cell division $K_{div}[dens]$. We conducted a local sensitivity analysis of the model to these parameters by changing their value by $\pm$ 30 and 50 % respectively to the reference value given in Table 8. For each condition, we ran 50 simulations starting from 700 cells drawn in a uniform law on $[0, z_{max}]$ and followed the evolution of TCP, MS and DR at steady state. For one set of parameters, to compute MS, we computed the time needed by a cell to cover the distance between $z = 40$ and $z = 175$ μm to avoid boundary effects. Namely, let t_f be the final time of simulation and $z_i(t)$ the position of cell i for $t \in [b_i, d_i]$ with b_i and d_i respectively the birth and death time of cell i (and $b_i = 0$ for a cell present at $t = 0$, and $d_i = t_f$ for cells still alive at $t = t_f$), we defined the start time $u_i = \inf\{t \in [b_i, d_i] : z_i(t) \in [40, 175]\}$ and the exit time $e_i = \sup\{t \in [b_i, d_i] : z_i(t) \in [40, 175]\}$. Eventually, setting $T_i = e_i - u_i$ and $Z_i = z_i(e_i) - z_i(u_i)$, the migration speed of cell i was defined as the ratio $\frac{Z_i}{T_i}$. Note that this speed does not necessarily match the fastest or the lowest speed reached by cell i during the simulation. The division rate of cell i is $\frac{n_{div,i}}{d_i - b_i}$ with $n_{div,i}$ the number of divisions of cell i. We then computed the average of these values among cells at steady state (after $t = 300$ h) for one realization of the PDMP, and then averaged over the 50 realizations to obtain respectively MS and DR. The TCP is taken at final time and averaged over the 50 realizations of the PDMP.

The effect of the three parameters tested is shown in Fig. 5. We observe that TCP is particularly impacted by the sensitivity of the division rate to local cell density: it shows a linear dependence to the $K_{div}[dens]$ parameter. In contrast, the extrusion rate and the repulsion force intensity have much lighter, and negative, effect.

On the contrary, the three parameters show a very similar influence on MS. Increasing the repulsion force, the extrusion rate or the division sensitivity all result in a comparable increase of cell velocity. A marked drop of the migration speed is however observed when the sensitivity of the division to local cell density is strongly reduced due to a specific behavior explained in Appendix D. The mechanisms by which the migration speed is increased seem however different. Increasing the repulsion force directly impacts mechanical interactions all along the crypt, so that cells move faster when they are not at mechanical equilibrium. By contrast, a higher $K_{div}[dens]$ results in a higher division rate leading to a higher cell density in the bottom of the crypt and thus pushing the whole cells upward. A higher q_{ex}^{∞} has a similar effect by depleting the cell density in the upper crypt. The greater number of cells for higher values of $K_{div}[dens]$ also increases the intensity of mechanical interactions. DR exhibits the same dependence to the three parameters as MS. This is expected because at steady-state, the total number of cells is almost constant (Fig. 4c) and therefore divisions must keep up with the migration to maintain the population.

Therefore, q_{ex}^{∞} and k_a seem to increase the activity of the epithelium, i.e. the migration speed and the number of divisions, while maintaining a constant population. On the contrary, $K_{div}[dens]$ strongly impacts the total cell population together with the epithelial activity.

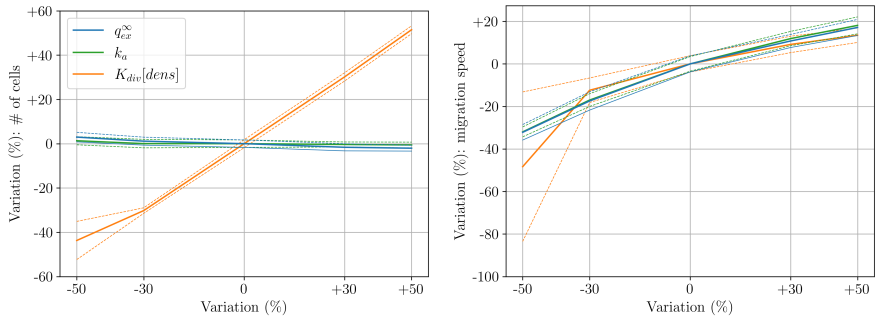

(a) Number of cells (TCP)

(b) Migration speed (MS)

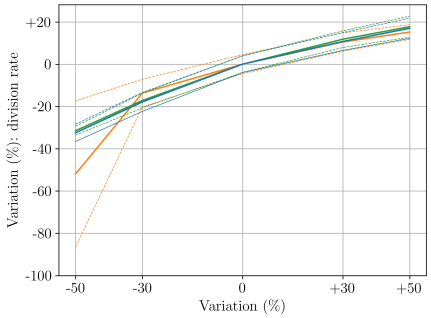

(c) Division rate (DR)

Number of cells (TCP)	725
Migration speed (MS)	1.28 $\mu m/h^{-1}$
Division rate (DR)	$3.6 \times 10^{-3} h^{-1}$

(d) Values for standard parameters

Fig. 5: **Local sensitivity analysis of hallmark of crypt physiology to the driving parameters.** Three parameters that potentialy impact the total number of cells at final time, the migration speed and the number of divisions in the crypt at steady state are tested. Parameters are shifted one by one, and model output variations are plotted. Mean (plain) and standard deviation (dashed lines) from 50 repetitions are plotted.

4.3 Spatial distribution and cell turn-over in the crypt

We now add cell types to the previous model. The 5 different cell types and cell differenciation events described in Sect. 2 are introduced, with the objective to reproduce the population size of each epithelial cell type in the crypt as well as their spatial distribution, as explained in Sect. 1.1 and depicted in Fig. 1a. We assume that there is a uniform concentration of butyrate in the crypt, so that cell differencation rates only depend on spatial and density terms. The precise jump rates we use are detailed in Appendix A.1 and summarized in Table 2. Parameter values are given in Table 9. We ran 50 independent simulations starting from an initial condition where cells are already spatially organised according to their types. For each simulation, positions of the 12 DCS cells are drawn randomly according to the following linear decreasing probability density

$$\rho_{dcs}(z)dz = \begin{cases} \frac{2}{12}(1-\frac{z}{12}) & \text{if } z \leq 12, \\ 0 & \text{otherwise.} \end{cases} \tag{25}$$

We can observe that the population of each cell types rapidly reaches a steady state after about 4 days (Fig. 6a). These steady state population levels match particularly well available biological data for the distal colonic crypt of mice (see Table 3). Total cell number, number of stem cells, and cell type ratios are correctly recovered, showing that our model is able to capture the phenomena insuring the population level regulations. Moreover, the spatial distribution of each cell types in the crypt also reproduces the typical spatial organization of a crypt described in Sect. 1.1 (Fig. 6b). The stem cells remain in the distal part of the crypt ($z \leq 20\mu m$), replaced upward by progenitor cells that are mainly located under $z \leq 80\mu m$. Then progenitor cells are progressively replaced for $z \geq 50\mu m$ by goblet cells and enterocytes, with the approximative ratio 1 : 3. DCS cells are kept in the stem cell niche ($z \leq 20\mu m$).

We also evaluate the renewal of the epithelium. To do so, we mimic the experimental procedure which relies on labeling mitotic cells and tracking their elimination over time [24]. We label at steady-state ($t = 800h$) the stem and progenitor cells, and we screen over time the ratio of labeled cells that have been eliminated respectively to the number of initially labeled cells. Upon division of a labeled cell, the label is randomly passed to the mother or the daughter cell with probability $p = 0.5$. We observe a fast renewal of epithelial cells (Fig. 7): after 2 days, on average 66% of labeled cells have been extruded, and it rises to 95% after 3.6 days. This is in agreement with experimental values for the renewal time of the mouse colonic epithelium which is 2.67 ± 2.04 days [24]. The migration speed is below reported experimental value. However, the reference values we use here for our observables come from different experiments which might explain some of the discrepancies.

We also note that the renewal rate seems to reach a plateau above 95% in our model, indicating that a small part of the cells retain their label and divide rarely. This is due to the fact that a portion of the stem cells in the lowest part of the crypt can neither move nor divide, due to contact inhibition and to the pressure exerted by the dividing cells higher in the crypt. We can see that about 17% of the stem cells are renewed (Fig. 7, blue curve) if we only label the stem cells, and that the average

	Regulation pathway (j)	
Jump index (k)	Wnt $[z]$	density $[dens]$
div, sc	−	−
div, pc	−	−
sc, pc	+	∅
pc, gc	+	∅
pc, ent	+	∅
ex, gc	+	+
ex, ent	+	+

Table 2: **Regulation of cell fate events used in Sect. 4.3.**

Observable	Simulated value	Reference value	Reference
total number of cells	694 ± 21 (at t_f)	700	[49]
number of stem cells	23 ± 7 (at t_f)	20	[59]
ratio of progenitors/total	0.22 ± 0.01 (at t_f)	0.22 (human)	[13]
ratio goblets/enterocytes	0.33 ± 0.03 (at t_f)	0.33	[69]
95 % renewal time (day)	3.6 ± 0.02	2.67 ± 2.04	[24]
division rate of stem cells (h^{-1})	$1/83 \pm 1/83$	1/24(SI)-1/62	[9,69]
division rates of progenitors (h^{-1})	$1/18 \pm 0$	1/12(SI)-1/62	[10,69]
migration speed ($\mu m/h$)	2.6 ± 0.03	4	[49]

Table 3: **Simulations results and experimental reference for the submodel of Sect. 4.3,** mean of 50 simulations, $t_f = 1000h$. SI = small intestine.

division rate of stem cells in our simulations is lower than for *in vivo* observations (Table 3). However, the latter lays within the simulated standard deviation interval. Progenitors average division rate is higher that experimental observation, but closer than for stem cells. As stem cells and progenitor cells influence each other, this is partially explained by the low division rate of stem cells. The variation of the stem cells renewal rate (Fig. 7) can be partly explained by the variation of the DCS cells positions. Indeed, at the beginning of each simulation these positions are drawn randomly in the distribution (25). DCS cells will then both impact contact inhibition of the stem cells and protect the stem cell niche from an invasion by the rapidly dividing progenitor cells accordingly.

4.4 Reproduction of the butyrate and O_2 gradient.

In the previous section, the spatial distribution of epithelial cells in the crypt was reproduced based on physical interactions between cells and spatial regulation, discarding cell metabolism. We now add butyrate and oxygen concentrations, whose dynamics follow equations (6,9) and (6,10) respectively, including the cell consumption in the source terms. The corresponding parameters are given in Table 10. The derivation of the chemical kinetics parameters is detailed in Appendix E.1. We do not yet take into account the feedback of butyrate on cell fate events (that is to say we use the exact same jump rates as in Sect.4.3, see Table 2 and Appendix A.1).

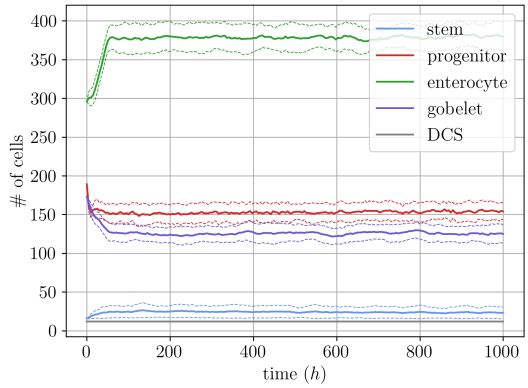

(a) **Composition of the epithelium**. Time evolution of the cell populations are displayed. The mean (plain) and standard deviation (dashed lines) from 50 repetitions are plotted.

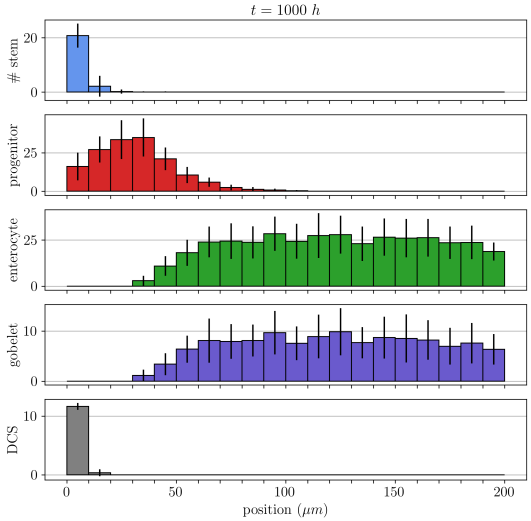

(b) **Spatial distribution of cell types at steady state**. Histograms of local cell counts are displayed, with mean and standard deviation from 50 simulations

Fig. 6: **Crypt structure.** The structure of the crypt by cell type is studied, by displaying the time evolution of the cell populations, and their spatial distribution at final time.

At first, we aimed at reproducing the gradient of dioxygen and butyrate observed in the crypt at homeostasis. We ran 50 independent simulations starting from an initial condition where the number of cells from each cell type corresponds to the average number obtained at steady-state in Sect. 4.3, and position of cells were randomly drawn from the average steady-state distribution of their cell type obtained in Sect.

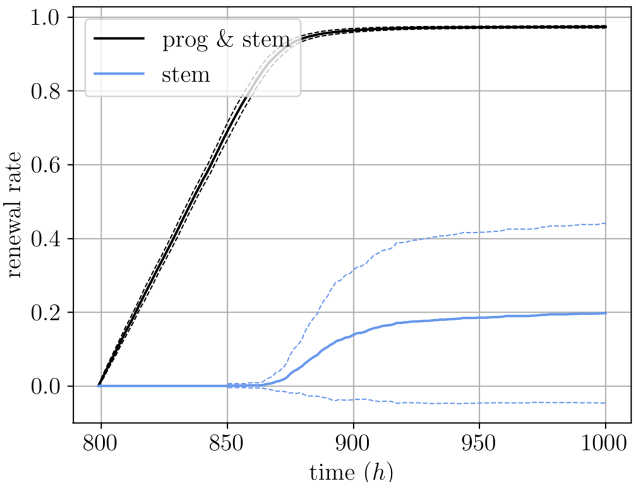

Fig. 7: **Renewal of the epithelium.** Fraction of labeled cells that have been eliminated among the pool of initially labeled cells. The mean (plain) and standard deviation (dashed lines) from 50 repetitions are displayed.

4.3 (and plotted in Fig. 6). Initial concentrations of butyrate and oxygen were respectively linearly increasing and decreasing with z. Concentrations of butyrate and O_2 obtained are plotted in Fig. 8. There is a strong spatial gradient of concentration for both molecules, due to the consumption by differentiated cells in the upper part of the crypt. Oxygen concentration decreases with z from 10 *au* at the bottom of the crypt to 1 *au* at the top while butyrate concentration increases from around 1 *mM* in the stem cell niche to 5 *mM* at the top. Few validation criteria are available for these results as concentrations cannot yet be measured precisely experimentaly in the crypt, despite being considered to play a major role in crypt organization. We used the fact that concentration of O_2 at the top of the crypt is around 10 times lower than at the bottom, as reported in [54]. This ratio of 10:1 is what we observe in our simulations, along with a concentration gradient of butyrate. These results confirm the hypothesis that the metabolism of differentiated epithelial cells in the upper part of the crypt induce a concentration gradient of butyrate at homeostasis and protect stem cells from deleterious effects of butyrate [32,63]. In vitro experiments have shown that a 1 *mM* concentration of butyrate is sufficient to strongly inhibit stem cells and progenitors proliferation [32]. In our model, the concentration of butyrate in the stem cell niche is 0.9 *mM*. To explain this value close to the inhibition value, one can argue that the experiments we mention were conducted in vitro. On the other hand, our model might overestimate the concentration of butyrate as we did not take into account the ketone production which is another metabolic pathway of butyrate consumption that does not involve oxygen [18].

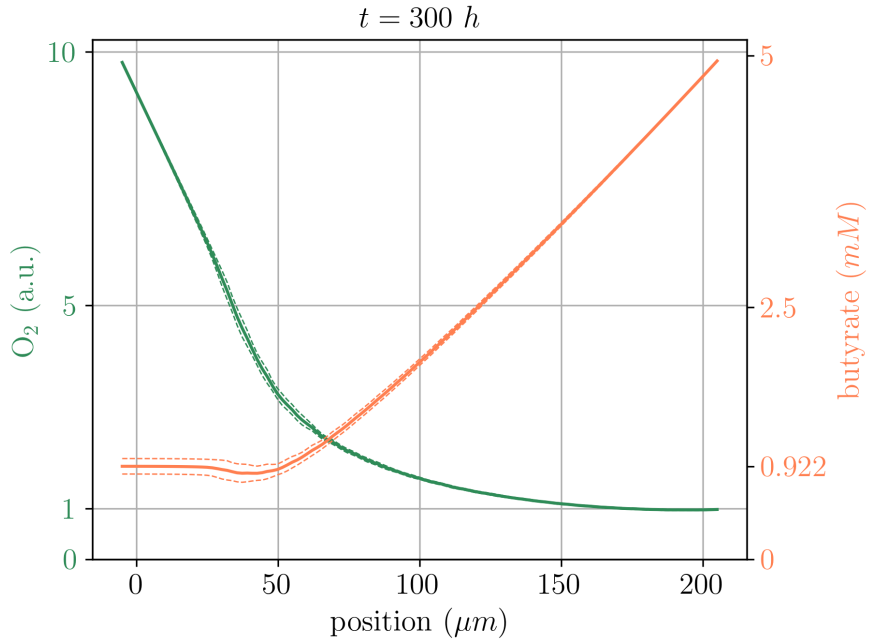

Fig. 8: **Concentration of O_2 and butyrate at homeostasis.** The mean (plain) and standard deviation (dashed lines) from 50 repetitions are plotted. Concentrations are expressed in *mM* for butyrate and in arbitrary units (a.u.) for oxygen, meaning that oxygen concentrations are normalized (see Appendix E.1).

4.5 Complete model

Finally, we simulated the complete IBM model described in Sect. 2, which takes into account the effect of butyrate on the rates of stem cell division and progenitor differentiation as summarized in Table 1. We assessed that the capability to reproduce the homeostatic crypt is conserved, regardless of the additional mechanism that is added. We ran 50 independent simulations using the same initial condition as in Sect. 4.4. In figure 9, we plotted the trajectories of some individual cells. We observe the expected behaviour of birth and proliferation at the bottom of the crypt, followed by differenciation and then extrusion along their migration to the top of the crypt. Figure 10 represents cells repartitions, numbers, and butyrate and oxygen concentrations. Figure 10c represents the renewal rate of the epithelium. Simulation results are summarized in Table 4. We observe a good recovery of the total number of cells, the different cell population ratios and the concentration gradients (Fig. 10 and Table 4), except for the number of progenitors which is higher than expected. The division rate of progenitors is still in the experimental range, and interestingly, the division rate of stem cells is improved compared to Sect. 4.3 and within experimental range (Table 4). The renewal of the epithelium (Fig. 10c) is however slower than in Sect. 4.3 and

Observable	Simulated value	Reference value	Reference
total number of cells	694 ± 22 (at t_f)	700	[49]
number of stem cells	17 ± 8 (at t_f)	20	[59]
ratio of progenitors/total	0.26 ± 0.02 (at t_f)	0.22 (human)	[13]
ratio goblets/enterocytes	0.32 ± 0.03 (at t_f)	0.33	[69]
90% renewal time (day)	6.6 ± 0.03	2.67 ± 2.04	[24]
division rate of stem cells (h^{-1})	$1/47 \pm 1/76$	1/24(SI)-1/62	[9,69]
division rates of progenitors (h^{-1})	$1/20 \pm 0$	1/12(SI)-1/62	[10,69]
ratio of O_2 concentration at bottom/at top	9.9 ± 0.1	10	[54]
butyrate concentration at bottom (mM)	1.0 ± 0.1		
migration speed ($\mu m/h$)	2.6 ± 0.04	4	[49]

Table 4: **Simulations results and experimental reference for the complete IBM model (Sect. 4.5),** mean of 50 simulations, $t_f = 500h$, SI = small intestine.

than experimental values. This might be due to the excess of progenitor cells which increases cell density in the progenitor zone and therefore decreases the division rate.

Now, we investigate the effect of a lower availability of butyrate in the lumen, which mimics a dysbiotic situation where butyrate-producing bacteria are reduced. We changed the butyrate concentration at the top of the crypt $c_{b,lum}$, testing values from 0.1 to 5 mM (Fig. 11b). In this case, the O_2 concentration at the top of the crypt rises and doubles for a luminal butyrate concentration of 1 mM, meaning that the luminal part of the crypt becomes microaerobic. This kind of dysbiotic situation where butyrate concentration is low, oxygen is high and cell type composition of the epithelium is similar to homeostasis may occur after an antibiotic treatment [54].

All together, the complete model includes the main regulation mechanisms of crypt turn-over and renders accurately most of the main biomarkers of an healthy crypt at homeostasis. However, at this level of complexity, the IBM model becomes challenging to manipulate and the deterministic PDE limit model turns out useful.

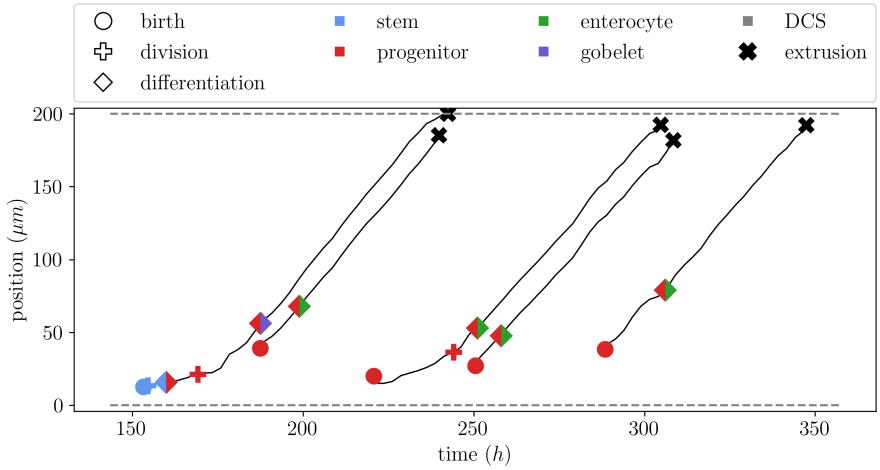

Fig. 9: **Example of individual cell trajectories in the complete model.** We represent 5 different cell trajectories computed by the complete model. The position of each cell is plotted respectively to time. Cell fate, i.e. stochastic events occurring to the cell, are represented by circle (birth), plus sign (division), square (differentiation) or cross (extrusion). Each symbol is color coded according to the cell type at event time. For differentiation, the square indicates the cell type before (leftmost part) and after (rightmost part) the stochastic jump.

5 Numerical exploration and analysis based on the deterministic approximation

5.1 Accuracy of the deterministic approximation

We aim to compare the outputs of the complete PDMP model with the deterministic approximation (21) derived in Sect. 3. The crypt homeostasis being described by the model steady states, we compare complete PDMP and its deterministic approximation when an equilibrium is reached. Starting from an empty crypt (i.e. $\rho_{l,0} = 0 \, \forall l \in \mathscr{T}$) and from a DCS cells distribution that approximates the distribution observed in the PDMP, the PDE approximation is simulated with a given boundary condition for the stem cells (see below) until steady state and compared to the PDMP outputs.

To approximate the DCS cells density found in the PDMP model, we chose the following shape :

$$\rho_{dcs}(z) = \frac{N_{dcs}}{\int_0^{z_{max}} \bar{\rho}_{dcs}(z)dz} \bar{\rho}_{dcs}(z) \tag{26}$$

with

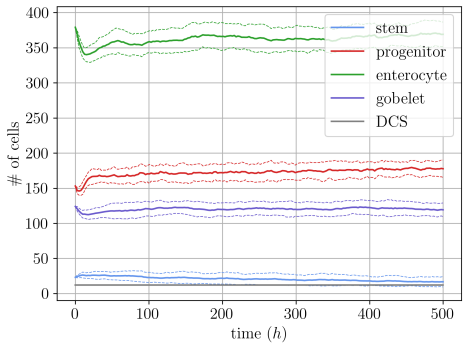

(a) **Composition of the epithelium**. Time evolution of the cell populations are displayed. The mean (plain) and standard deviation (dashed lines) from 50 repetitions are plotted.

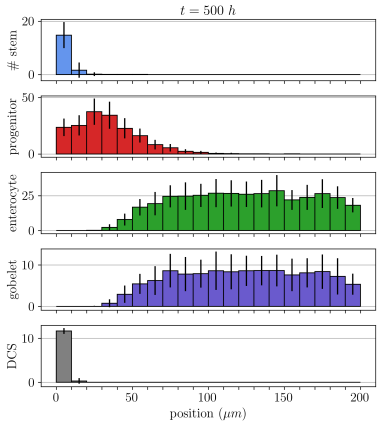

(b) **Spatial distribution of cell types at steady state**. Histograms of local cell counts are displayed, mean and standard deviation from 50 simulations.

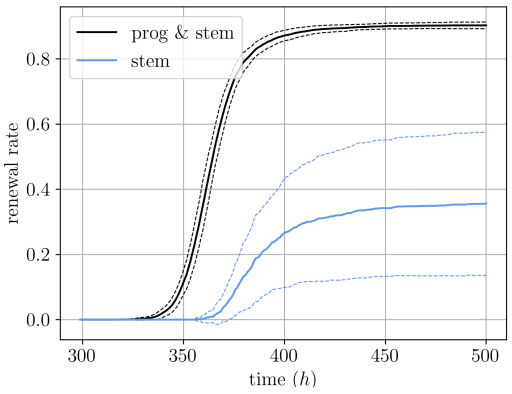

(c) **Renewal of the epithelium in the complete model.** Fraction of labeled cells that have been eliminated among the pool of initially labeled cells. Mean (plain) and standard deviation (dashed lines) from 50 repetitions.

Fig. 10: **Crypt structure and dynamic for the complete model.**

$$\bar{\rho}_{dcs}(z) = \begin{cases} d(z-z_d)+1 & \text{if } z_d - \frac{1}{d} < z < z_d, \\ 1 & \text{if } z_d \leq z \leq z_u, \\ 1+u(z-z_u) & \text{if } z_u < z < z_u - \frac{1}{u}, \\ 0 & \text{otherwise,} \end{cases}$$

where $z_d, d > 0, z_u, u < 0$ and N_{dcs} is the predefined number of DCS cells. This function is a piecewise-linear approximation of a step-function summing to N_{dcs}, controlled by 4 parameters (d, u, z_d, z_u). As the PDMP is far from the asymptotic con-

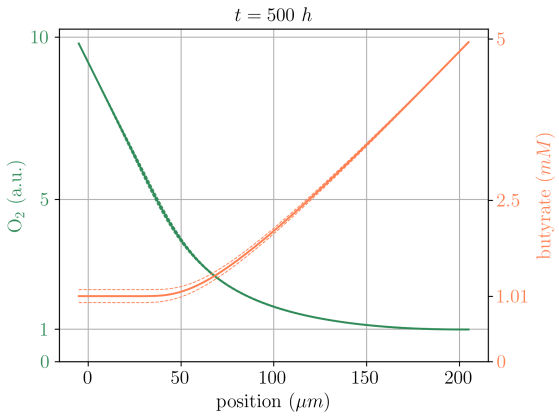

(a) **Concentration of O_2 and butyrate at homeostasis.** The mean (plain) and standard deviation (dashed lines) from 50 repetitions are plotted. Concentrations are expressed in mM for butyrate and in arbitrary units (a.u.) for oxygen, meaning that oxygen concentrations are normalized by a reference concentration of oxygen in the lumen at homeostasis.

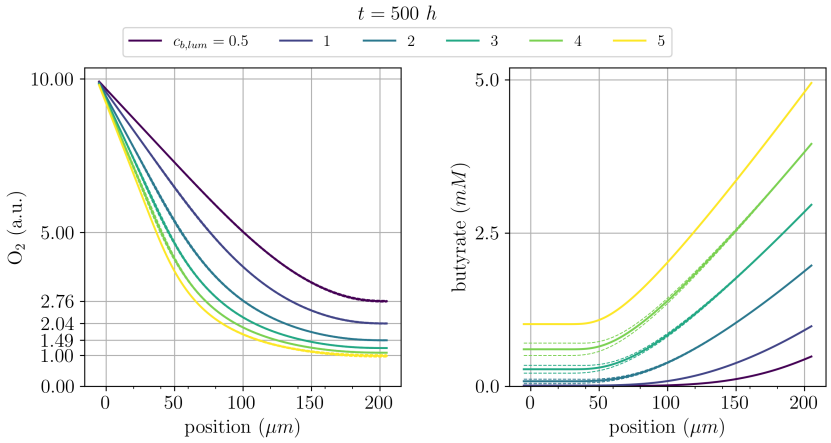

(b) **Effect of luminal concentration of butyrate $c_{b,lum}$.** O_2 and butyrate spatial distribution are displayed for varying luminal boundary condition for butyrate, from 0.5 to $5mM$. Mean (plain) and standard deviation (dashed lines) from 30 simulations

Fig. 11

dition (cell size close to zero) for which the approximation was derived, we adapted the values of these parameters, and additionally the values of W, D and γ_β^∞ as well as the boundary value for the stem cell density at the bottom, to obtain a reasonable fit of the mean cell distribution and concentration profiles predicted by the PDMP at steady state.

We observed that, although the DCS cells are "inactive" their shape and position influence cell distributions and proportions. When varying the values of (d, u, z_d,

z_u) which mimics the random draws of DCS cells in the PDMP model simulation, we observed that some parameter sets produced undesired behaviours such as no cell division at all. This is consistent with the high variability of stem cells renewal that we observed in the IBM model and that we attributed to the randomness of the DSC cells position. In certain cases, DSC cells blocked stem cells division by contact inhibition (see end of Sect. 4.3).

The parameters that provide a suitable approximation of the PDMP model are gathered in Table 12. They will be used for numerical simulation in the sequel. To compare PDMP and PME model behaviours, we display steady-state densities of cells for both models in Fig. 12. We furthermore display the comparison of cell fate events by plotting the right-hand side of Eq. (21), i.e. the spatialized rate of division, differentiation and extrusion at steady-state. The spatialization of the cell fate events of the PDMP is correctly recovered, with extrusion events at the top of the crypt, division events near the stem cell niche in the lower crypt, and differentiation events distributed along the first half of the crypt. Spatial distribution of cells and cell fate events of PME are in good agreement with the PDMP.

Limit model outputs are gathered in Table 5 and can be compared with the complete PDMP outputs in Table 4. We evaluate the average rate of the different cell fate events according to the following formula

$$\tau_k = \frac{\int_0^{z_{max}} \rho_l(z) q_k^\infty q_k(z, l, D \times \rho, c_b) dz}{\int_0^{z_{max}} \rho_l(z) dz} \tag{27}$$

for $(k, \rho_l) \in \{(div; sc, \rho_{sc}), (sc; pc, \rho_{sc}), (div; pc, \rho_{pc}), (pc; gc, \rho_{pc}), (pc; ent, \rho_{pc}),$ $(ex; gc, \rho_{gc}), (ex; ent, \rho_{ent})\}$. We observe that total cell and stem cells numbers are in the range of the PDMP results (709 vs 694 ± 22, and 20 vs 17 ± 8), as well as the ratio of globet cells/enterocytes (0.3 vs 0.32 ± 0.03) or stem cell division rate (0.036 vs 0.021 ± 0.013). Although progenitor cells division rate is in the right order (0.042 vs 0.05 ± 0.0) the ratio between progenitor and total cell numbers is lower (0.14 vs 0.26 ± 0.02). The parameters at our hand (DCS density shape, W, D, γ_β^∞ and boundary condition for the stem cells) do not allow an appropriate value while keeping a good fit for the other model observable in Table 5. Our sensitivity analysis in Sect. 5.2 confirmed that this was hardly achievable without modifying other parameter values in the model.

5.2 Sensitivity analysis

We use the deterministic approximation of the IBM to perform a Sensitivity Analysis (SA) using the global method of the Elementary Effects (EE) of Morris [44,56]. Indeed, this method uses variance-based techniques and exhibits reasonable computational time, which makes it suitable for SA on models with high number of inputs or with high computational load [17]. We briefly recall that Morris method estimates sensitivity indices by generating random trajectories in the (rescaled) parameter space Ω, such that along each trajectory, parameter values are changed one by one following a predefined variation Δ. More precisely, let $\mathbf{X} = (X_1, \cdots, X_p)$. For each trajectory k, we draw a random perturbation of the set of integers $\{1 \leq i \leq p\}$ denoted by

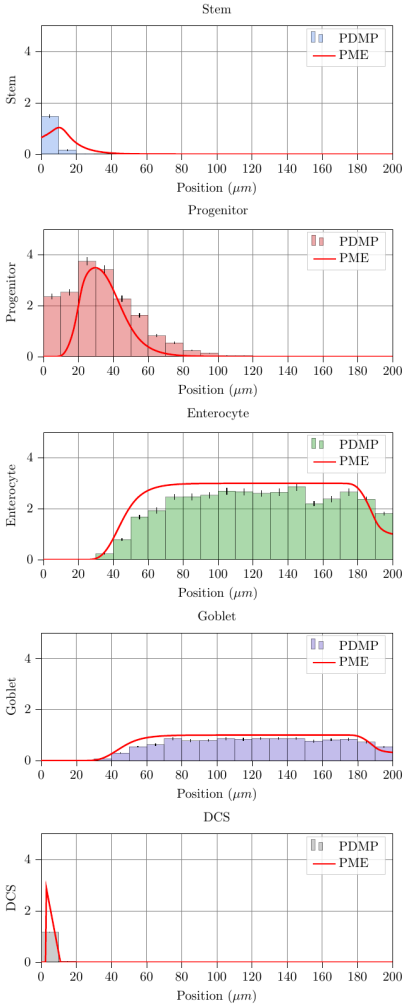

(a) Spatial distributions of densities

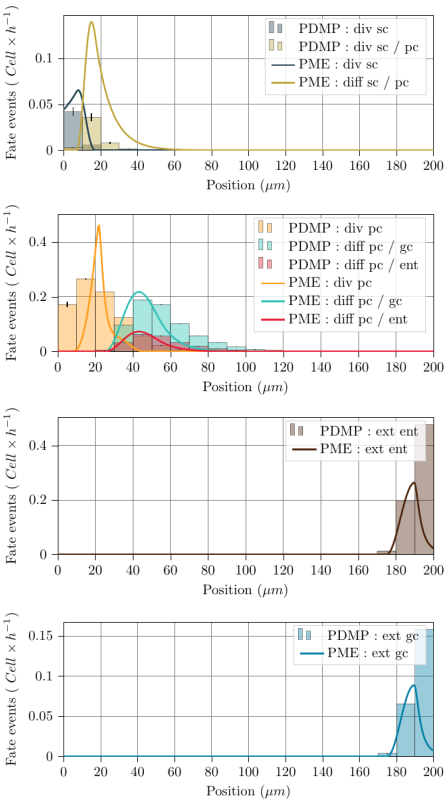

(b) Cell fate: spatial distribution of division, differentiation and extrusion rates.

Fig. 12: **Comparison of densities and cell fate events between PDMP and PME model at steady-state**. Results obtained using parameters from tables 12 and 9 for the PME. Concerning the PDMP, spatial distribution of cells (resp. cell fate events) are histograms of local cell (resp. jumps) counts with mean and standard deviation from the mean from 50 simulations.

Observable	Simulated value
Total number of cells	709
Number of stem cells	20
Ratio progenitors/total	0.14
Ratio goblets/enterocytes	0.3
Division rate of stem cells (h^{-1})	0.036
Differentiation rate of stem cells (h^{-1})	0.096
Division rate of progenitor cells (h^{-1})	0.042
Differentiation rate of progenitor cells in goblet cells (h^{-1})	0.017
Differentiation rate of progenitor cells in enterocytes (h^{-1})	0.051
Extrusion rate of goblet cells (h^{-1})	0.007
Extrusion rate of enterocytes (h^{-1})	0.007
Ratio of O_2 concentration at bottom/at top	9.78
Butyrate concentration at bottom (mM)	1.64

Table 5: Deterministic approximation model outputs.
See Eq. (27) for the formula used to compute rates.

$\{\sigma^k(i)\}$. Then, the i-th step of the trajectory k is, $\forall 1 \leq i \leq n$,

$$\mathbf{X}_i^k = (X_{1,0}^k + \mathbb{1}_{\{\sigma_k(1)\leq i\}} \times \Delta, \cdots, X_{p,0}^k + \mathbb{1}_{\{\sigma_k(p)\leq i\}} \times \Delta)$$

and $\mathbf{X}_0^k = (X_{1,0}^k, \cdots, X_{p,0}^k)$. According to [44], we used $\Delta = p/2(p-1)$ with $p = 4$. Each trajectory k allows to calculate the elementary effect EE_i^k of the parameter X_i on the output Y

$$EE_i^k = \frac{Y(\mathbf{X}_{\sigma(i)}^k) - Y(\mathbf{X}_{\sigma(i)-1}^k)}{\Delta}. \tag{28}$$

A sample distribution of EE values for each parameter is generated by simulating r trajectories with random starting points, from which the following sensitivity indices are computed for each parameter X_i

$$\mu_i = \frac{1}{r}\sum_{k=1}^{r} EE_i^k; \qquad \sigma_i = \sqrt{\frac{1}{r}\sum_{k=1}^{r}(EE_i^k - \mu_i)^2}; \qquad \mu_i^* = \frac{1}{r}\sum_{k=1}^{r}|EE_i^k|. \tag{29}$$

Indices are the mean μ_i, the standard deviation σ_i and the index μ_i^* proposed in [17] to avoid compensation of effects with opposite signs in the case of a non-monotonic influence. Following [6] (see Table 6) parameters can subsequently be classified by their effect (negligible, significant, non linear...) on the output of interest.

Effect	**Morris index**
Decreasing	$\mu < 0$
Increasing	$\mu > 0$
Negligible	$\mu^* \sim 0$ and $\sigma \sim 0$
Linear and additive	μ^* high and $\sigma \sim 0$
Non linear or non monotone	σ high
In interactions of order ≥ 2	σ high

Table 6: Morris index interpretation [6]

The output of the model selected for the SA were the total density of cells in the crypt, the division rate of progenitor cells and the ratio of O_2 concentration at the bottom and at the top of the crypt, as for the PDMP. To carry out the analysis we vary the parameters over a range of 50% of their value described in Tables 11 and 12 except for W which varies at 30%. Moreover, to select the number of trajectories r in order to obtain stable results, we applied two criteria given in [58]. The first criteria (Ranking) is close to 1 when the ranking of influential parameters is stabilized and the second (Screening) reaches values below 0.05 when the screening (separation between influential and non-influential parameters) is stable. The authors of [58] propose another criteria based on indices values, that we discarded because we are interested in large effects. We used two Python libraries, SALib and SAFE to conduct the SA [30,52].

Results of the sensitivity analysis are presented in Fig. 13. In the majority of cases the ranking and screening criteria thresholds are reached after running 600 trajectories. The only output for which criterion are not fulfilled is the ratio of O_2 concentration, due to the high number of parameters with a similar sensitivity index value. We plot the standard deviation of EEs σ as a function of μ^*, the mean of the absolute values. We recall that high values of μ^* indicate a high impact on the output, while high values of σ is representative of non-monotone or non-linear effects, or possible interaction with another parameter. Fig. 13 allows a better understanding of the effects of parameters on outputs.

The total density is mainly influenced by 2 groups of parameters. The first one gathers the most influential parameters. It is composed of regulation parameters with a positive effect ($K_{div,pc}[dens]$ as for the IBM model of Sect. 4.2, $K_{ext,gc}[z]$ and $K_{div,pc}[z]$). Parameters regulating progenitor cells division are particularly involved as progenitor cells are the main type of proliferating cells. Parameter W, which characterizes repulsion between cells, is also part of this group but it has a negative effect which is consistent with the influence of k_a on the PDMP model in Fig. 5. In the second group of still important but less influential parameters, we find parameters related to stem cells and concentration boundary conditions.

The division rate of progenitor cells is mainly influenced by W and $K_{div,pc}[z]$, results in line with those obtained for total density. When $K_{div,pc}[z]$ increases, progenitor cells differentiate higher in the crypt and therefore epithelial cells spend more time in a progenitor state. However, they don't make more divisions as most likely the epithelium is saturated and density inhibition is fully active. From there comes the negative impact of $K_{div,pc}[z]$ on the division rate. We also note that an increase of the butyrate concentration at the top of the crypt $c_{b,lum}$ has a positive effect on the division rate. This could be explained by a faster differentiation (stimulated by butyrate, see Table 1) of progenitor cells into goblet cells or enterocytes. As expected, stem cell parameters have a negative effect on progenitor cell due to the competition for space between progenitors and stem cells.

The ratio of O_2 concentration at the bottom and at the top of the crypt has a significant group of influential parameters.The abundance of parameters with close μ^* and σ values explains the non-convergence of the rank indices. These results highlight the influence of all parameters. The σ indices obtained are twice as large as the μ^* indices, which suggest strongly non-linear, non-monotonic or interactive behaviours. This was the case when running simulations.

One parameter in particular emerges from these analyses, W, which is present on the podium of each of these three outputs but also on a majority of those presented in Fig. 14. In sum we look at 20 different outputs : total density (ρ), density of each cell type (ρ_l), ratio of progenitor cells to total density, medium position ($\bar{z_l}$) see Eq (5.2), rate of cell fate events , concentration of O_2 (resp. Butyrate) at the top (resp. bottom) of the crypt, ratio of O_2 concentration (bottom/top). To visualize results of all the outputs on the same figure we normalized for each output the values μ_i^* of each parameter X_i by $max_i(\mu_i^*)$. We also indicated with a color code if their influence on the output is positive or negative according the the sign of μ_i. Like we said W influence many outputs, but others are also influential such as $K_{div,sc}[z], K_{div,pc}[z], K_{div,pc}[dens], K_{ext,gc}[z]$.

$$\bar{z_l} = \frac{\int_0^{Z_{max}} \rho_l(z,t) z dz}{\int_0^{Z_{max}} \rho_l(z,t) dz}$$

6 Discussion and perspective

A model of cell fate in the intestinal crypt, including interactions with microbiota-derived metabolites has been introduced and studied. We now discuss the new features included in the model. We finally raise and discuss model limitations.

6.1 A PDMP model of crypt dynamics, including interaction with the microbiota

The model hereby introduced adds up to a long list of models in the litterature studying the cell fate in the intestinal crypt. It however improves existing models in two ways. First, it provides new biological insights by focusing on interactions with the gut microbiota. Indeed, existing models mainly address issues related to morphogenesis or oncology: they then put a strong effort on modeling mechanical and biological mechanisms involved in cell turn-over and crypt formation. In this study, we rather focus on regulations of the crypt homeostasis that involve important interactions with the microbiota. These interactions, secondary for morphogenesis or abnormal crypt development during cancer, are crucial at homeostasis: in an healthy crypt, microbe-derived metabolites such as butyrate are used by the colonocytes as energetic source, the metabolism of which consumes oxygen and maintains anaerobia in the intestinal lumen. This microaerobic environment is beneficial for butyrate-producing microorganisms. In our model, the butyrate concentration presents a strong gradient in the crypt and we estimate the concentration of butyrate at the bottom of the crypt to be around 1 mM. This concentration gradient is commonly used as a working hypothesis, but it cannot be properly measured in vivo yet. Our model seems however to favour this hypothesis. Moreover, we could estimate the relationship between the butyrate and the O_2 concentrations at the top of the crypt. A microaerobic situation (doubling of the O_2 concentration from homeostasis) was reached at a luminal butyrate concentration of 1 mM.

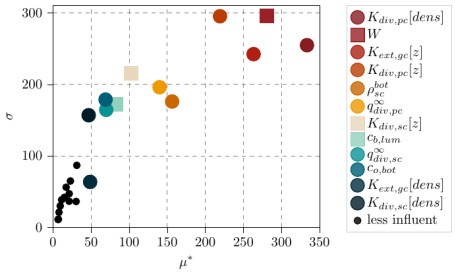

(a) Sensitivity analysis indices σ against μ^* for the **total density** of cells in the crypt.

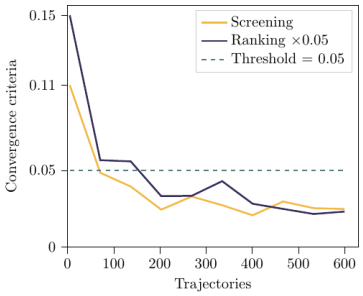

(b) Ranking and screening indices convergence for the **total density** of cells in the crypt.

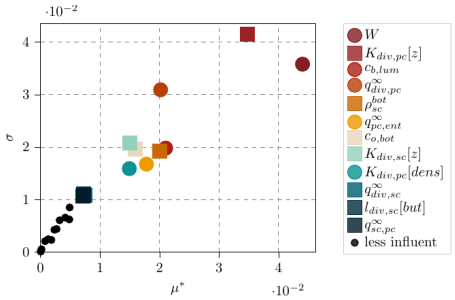

(c) Sensitivity analysis indices σ against μ^* for the **division rate of progenitor cells**.

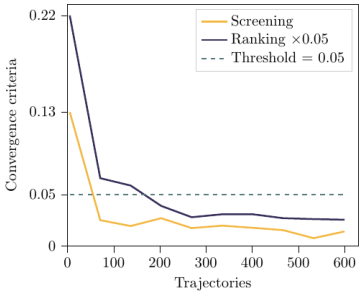

(d) Ranking and screening indices convergence for the **division rate of progenitor cells**.

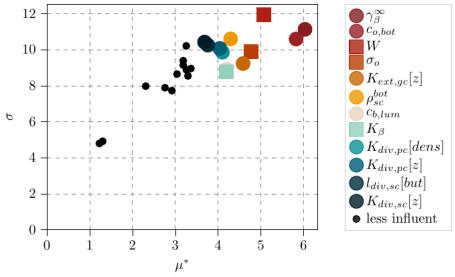

(e) Sensitivity analysis indices σ against μ^* for the **ratio of O_2 concentration (bottom/top)**.

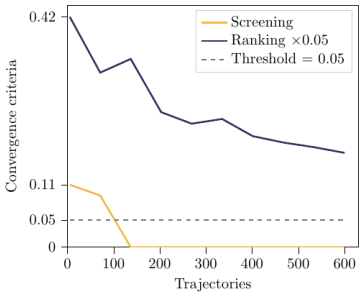

(f) Ranking and screening indices convergence for **the ratio of O_2 concentration (bottom/top)**.

Fig. 13: **Sensitivity analysis results and ranking indices** Figures on the left represent the standard deviation of EEs against the mean of absolute values of EEs. Parameters are listed in order of influence (circle: increasing effect ; square: decreasing effects). On the right we represent the criteria convergence with a threshold represented by the dashed lines. We recall that convergences are obtained if the ranking index is below 1 and screening below 0.05 based on the work of ([58]). In order to make the convergences visibly comparable, the ranking index is multiplied by 0.05 to share the same threshold as the screening index.

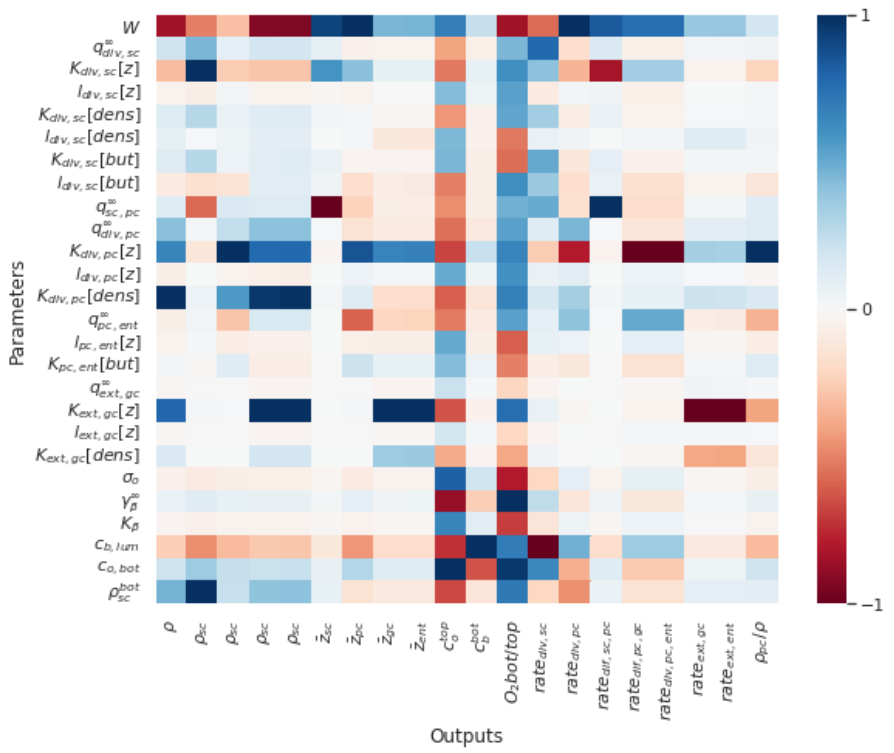

Fig. 14: **Visualization of SA results on different outputs** The heat map values are based on the normalize μ_i^* index by $max_i(\mu_i^*)$ for each parameter X_i. We use the sign of μ_i to determine whether the parameter influence is positive (red) or negative (blue). The more influential a parameter is, the darker the corresponding colour (red or blue).

Second, along with the model, a rigorous mathematical framework has been proposed based on PDMPs, which is in itself a novelty for a crypt model. This framework allows for a theoretical analysis of the system. In particular, it ensures the well-posedness of the model, guarantying locally bounded positive solutions. Furthermore, asymptotic analysis arguments lead to the formal derivation of a limit deterministic model of the PDMP. This limit model facilitates and fasten the numerical exploration of the system, by replacing multiple replicates of the same stochastic IBM by one unique deterministic simulation of an approximate average solution.

An extensive numerical exploration of both models (the PDMP model and its deterministic approximation) has been conducted and allowed identifying the main parameters driving different outputs, among them total cell population, progenitor divisions and O_2 distribution. This numerical exploration provides a complete overview of the main model drivers. Interestingly, it suggest that the top/bottom ratio of oxygen in the crypt is highly sensitive to a large number of parameters, among which cell

related parameters, with a complex, nonlinear dependence. This highlights the role of crypt cells in the maintenance of anaerobic conditions in the gut.

6.2 Improving microbiota integration and mathematical analysis

In this model, the impact of microbe-derived metabolites on the crypt physiology has been added, with in particular the oxygen consumption that drives luminal anaerobia beneficial for the main part of commensals. If the most important mechanisms mediating the interactions between the host and the microbiota have been taken into account, the microbial populations were not modeled in themselves in this study. In the future, a microbial compartment should be added to accurately model butyrate production in an anaerobic environment and oxygen harmful impact on bacterial populations. This crypt model could also be embedded in macroscopic model of gut physiology, such as for example in [12, 35].

To include the impact of the microbe-derived metabolites we chose to decrease the complexity of other mechanisms such as the mechanical interactions. Some crypt models, for instance [15], involve a very detailed biophysical models of cell-cell interactions that are crucial for studying crypt morphogenesis or hyperplasia. However, we chose to simplify the description of the mechanics in order to reduce the computational load that was placed instead on the description of butyrate regulations. It also allowed a simpler derivation of the self-aggregation limit model. This simplified version of the mechanical interactions however rendered accurately the main biomarkers of an healthy crypt, in particular migration speed, renewal rate or spatial structure.

Another potential improvement of the present study would be a rigorous derivation of the PME limit model. In this paper, we limited ourselves to a formal derivation, focusing on the main simplifications leading to the limit. To our knowledge, a rigorous derivation of the PME from the self-aggregation model is still an open problem.

All together, this model provides an important brick for modeling microb-host symbiosis and crypt homeostasis. It could be used to study specifically the interplay between microbial metabolism and host cell turnover, which is crucial for epithelial maturation and microbiota.

References

1. Butyrate and bioactive proteolytic form of Wnt-5a regulate colonic epithelial proliferation and spatial development. Scientific Reports **6**(August), 1–12 (2016). DOI 10.1038/srep32094
2. Virulence factors enhance Citrobacter rodentium expansion through aerobic respiration. Science **353**(6305), 1249–1253 (2016). DOI 10.1126/science.aag3042
3. Alex, S., Lange, K., Amolo, T., Grinstead, J.S., Haakonsson, A.K., Szalowska, E., Koppen, A., Mudde, K., Haenen, D., Al-Lahham, S., Roelofsen, H., Houtman, R., van der Burg, B., Mandrup, S., Bonvin, A.M.J.J., Kalkhoven, E., Muller, M., Hooiveld, G.J., Kersten, S.: Short-Chain Fatty Acids Stimulate Angiopoietin-Like 4 Synthesis in Human Colon Adenocarcinoma Cells by Activating Peroxisome Proliferator-Activated Receptor. Molecular and Cellular Biology **33**(7), 1303–1316 (2013). DOI 10.1128/MCB.00858-12. URL `http://mcb.asm.org/cgi/doi/10.1128/MCB.00858-12`
4. Almet, A.A., Maini, P.K., Moulton, D.E., Byrne, H.M.: Modeling perspectives on the intestinal crypt, a canonical system for growth, mechanics, and remodeling. Current Opinion in Biomedical Engineering **15**, 32–39 (2020)

5. Aregba-Driollet, D., Natalini, R., Tang, S.: Explicit diffusive kinetic schemes for nonlinear degenerate parabolic systems. Mathematics of Computation **73**(245), 63–94 (2003). DOI 10.1090/S0025-5718-03-01549-7. URL http://www.ams.org/mcom/2004-73-245/S0025-5718-03-01549-7/
6. Awad, M., Senga Kiesse, T., Assaghir, Z., Ventura, A.: Convergence of sensitivity analysis methods for evaluating combined influences of model inputs. Reliability Engineering & System Safety **189**, 109–122 (2019). DOI 10.1016/j.ress.2019.03.050. URL https://linkinghub.elsevier.com/retrieve/pii/S0951832018305763
7. Bansaye, V., Méléard, S.: Stochastic models for structured populations: scaling limits and long time behavior. Springer International Publishing (2015)
8. Barker, N.: Adult intestinal stem cells: Critical drivers of epithelial homeostasis and regeneration. Nature Reviews Molecular Cell Biology **15**(1), 19–33 (2014). DOI 10.1038/nrm3721. URL http://dx.doi.org/10.1038/nrm3721
9. Barker, N., van Es, J.H., Kuipers, J., Kujala, P., van den Born, M., Cozijnsen, M., Haegebarth, A., Korving, J., Begthel, H., Peters, P.J., Clevers, H.: Identification of stem cells in small intestine and colon by marker gene Lgr5. Nature **449**(7165), 1003–1007 (2007). DOI 10.1038/nature06196. URL http://www.nature.com/articles/nature06196
10. Barker, N., van de Wetering, M., Clevers, H.: The intestinal stem cell. Genes & Development **22**(14), 1856–1864 (2008). DOI 10.1101/gad.1674008. URL http://www.genesdev.org/cgi/doi/10.1101/gad.1674008
11. Batlle, E., Henderson, J.T., Beghtel, H., Van den Born, M.M., Sancho, E., Huls, G., Meeldijk, J., Robertson, J., Van de Wetering, M., Pawson, T., Clevers, H.: β-catenin and TCF mediate cell positioning in the intestinal epithelium by controlling the expression of EphB/EphrinB. Cell **111**(2), 251–263 (2002). DOI 10.1016/S0092-8674(02)01015-2
12. Bourgin, M., Labarthe, S., Kriaa, A., Lhomme, M., Gérard, P., Lesnik, P., Laroche, B., Maguin, E., Rhimi, M.: Exploring the bacterial impact on cholesterol cycle: A numerical study. Frontiers in Microbiology **11**, 1121 (2020)
13. Bravo, R., Axelrod, D.E.: A calibrated agent-based computer model of stochastic cell dynamics in normal human colon crypts useful for in silico experiments. Theoretical Biology and Medical Modelling **10**(1), 66 (2013)
14. Buckwar, E., Riedler, M.G.: An exact stochastic hybrid model of excitable membranes including spatio-temporal evolution. Journal of mathematical biology **63**(6), 1051–1093 (2011)
15. Buske, P., Przybilla, J., Loeffler, M., Sachs, N., Sato, T., Clevers, H., Galle, J.: On the biomechanics of stem cell niche formation in the gut - Modelling growing organoids. FEBS Journal **279**(18), 3475–3487 (2012). DOI 10.1111/j.1742-4658.2012.08646.x
16. Byndloss, M.X., Bäumler, A.J.: The germ-organ theory of non-communicable diseases. Nature Reviews Microbiology **16**(2), 103–110 (2018). DOI 10.1038/nrmicro.2017.158. URL http://www.nature.com/doifinder/10.1038/nrmicro.2017.158
17. Campolongo, F., Cariboni, J., Saltelli, A.: An effective screening design for sensitivity analysis of large models. Environmental Modelling & Software **22**(10), 1509–1518 (2007). DOI 10.1016/j.envsoft.2006.10.004. URL https://linkinghub.elsevier.com/retrieve/pii/S1364815206002805
18. Cherbuy, C., Darcy-Vrillon, B., Morel, M.T., Pégorier, J.P., Duée, P.H.: Effect of germfree state on the capacities of isolated rat colonocytes to metabolize n-Butyrate, glucose, and glutamine. Gastroenterology **109**(6), 1890–1899 (1995). DOI 10.1016/0016-5085(95)90756-4. URL https://linkinghub.elsevier.com/retrieve/pii/0016508595907564. **
19. Clausen, M.R., Mortensen, P.B.: Kinetic studies on the metabolism of short-chain fatty acids and glucose by isolated rat colonocytes. Gastroenterology **106**(2), 423–432 (1994). DOI 10.1016/0016-5085(94)90601-7
20. Cremer, J., Arnoldini, M., Hwa, T.: Effect of water flow and chemical environment on microbiota growth and composition in the human colon. Proceedings of the National Academy of Sciences **114**(25), 6438–6443 (2017)
21. Curtain, R.F., Zwart, H.J.: An introduction to infinite dimensional linear systems theory. Springer (1995)
22. Daley, D.J., Vere-Jones, D.: An Introduction to the Theory of Point Processes. Probability and Its Applications. Springer (2003, second edition). URL https://books.google.fr/books?id=GqRXYFxe0l0C
23. Darrigade, L.: Modélisation du dialogue hôte-microbiote au voisinage de l'épithélium de l'intestin distal. Ph.D. thesis, université Paris-Saclay (2020)

24. Darwich, A.S., Aslam, U., Ashcroft, D.M., Rostami-Hodjegan, A.: Meta-analysis of the turnover of intestinal epithelia in preclinical animal species and humans. Drug Metabolism and Disposition **42**(12), 2016–2022 (2014). DOI 10.1124/dmd.114.058404
25. Degirmenci, B., Valenta, T., Dimitrieva, S., Hausmann, G., Basler, K.: GLI1-expressing mesenchymal cells form the essential Wnt-secreting niche for colon stem cells. Nature (2018). DOI 10.1038/s41586-018-0190-3. URL http://dx.doi.org/10.1038/s41586-018-0190-3http://www.nature.com/articles/s41586-018-0190-3
26. Fan, Y.Y., Davidson, L.A., Callaway, E.S., Wright, G.A., Safe, S., Chapkin, R.S.: A bioassay to measure energy metabolism in mouse colonic crypts, organoids, and sorted stem cells. American Journal of Physiology - Gastrointestinal and Liver Physiology **309**(1), G1–G9 (2015). DOI 10.1152/ajpgi.00052.2015. URL http://ajpgi.physiology.org/lookup/doi/10.1152/ajpgi.00052.2015
27. Fletcher, A.G., Murray, P.J., Maini, P.K.: Multiscale modelling of intestinal crypt organization and carcinogenesis. Mathematical Models and Methods in Applied Sciences **25**(13), 2563–2585 (2015). DOI 10.1142/S0218202515400187. URL http://www.worldscientific.com/doi/abs/10.1142/S0218202515400187
28. Hannezo, E., Coucke, A., Joanny, J.F.: Interplay of migratory and division forces as a generic mechanism for stem cell patterns. Physical Review E **93**(2), 022405 (2016). DOI 10.1103/PhysRevE.93.022405. URL https://link.aps.org/doi/10.1103/PhysRevE.93.022405
29. Hannezo, E., Prost, J., Joanny, J.F.: Instabilities of Monolayered Epithelia: Shape and Structure of Villi and Crypts. Physical Review Letters **107**(7), 078104 (2011). DOI 10.1103/PhysRevLett.107.078104. URL https://link.aps.org/doi/10.1103/PhysRevLett.107.078104
30. Herman, J., Usher, W.: SALib: An open-source Python library for Sensitivity Analysis. The Journal of Open Source Software **2**(9), 97 (2017). DOI 10.21105/joss.00097. URL http://joss.theoj.org/papers/10.21105/joss.00097
31. Jacobsen, M.: Point process theory and applications: marked point and piecewise deterministic processes. Birkhaüser (2006)
32. Kaiko, G.E., Ryu, S.H., Koues, O.I., Collins, P.L., Solnica-Krezel, L., Pearce, E.J., Pearce, E.L., Oltz, E.M., Stappenbeck, T.S.: The Colonic Crypt Protects Stem Cells from Microbiota-Derived Metabolites. Cell **165**(7), 1708–1720 (2016). DOI 10.1016/j.cell.2016.05.018. URL http://dx.doi.org/10.1016/j.cell.2016.05.018
33. Kelly, C.J., Zheng, L., Campbell, E.L., Saeedi, B., Scholz, C.C., Bayless, A.J., Wilson, K.E., Glover, L.E., Kominsky, D.J., Magnuson, A., Weir, T.L., Ehrentraut, S.F., Pickel, C., Kuhn, K.A., Lanis, J.M., Nguyen, V., Taylor, C.T., Colgan, S.P.: Crosstalk between microbiota-derived short-chain fatty acids and intestinal epithelial HIF augments tissue barrier function. Cell Host and Microbe **17**(5), 662–671 (2015). DOI 10.1016/j.chom.2015.03.005. URL http://dx.doi.org/10.1016/j.chom.2015.03.005
34. Krndija, D., El Marjou, F., Guirao, B., Richon, S., Leroy, O., Bellaiche, Y., Hannezo, E., Matic Vignjevic, D.: Active cell migration is critical for steady-state epithelial turnover in the gut. Science **365**(6454), 705–710 (2019). DOI 10.1126/science.aau3429. URL http://www.sciencemag.org/lookup/doi/10.1126/science.aau3429
35. Labarthe, S., Polizzi, B., Phan, T., Goudon, T., Ribot, M., Laroche, B.: A mathematical model to investigate the key drivers of the biogeography of the colon microbiota. Journal of Theoretical Biology **462**, 552–581 (2019). DOI https://doi.org/10.1016/j.jtbi.2018.12.009. URL https://www.sciencedirect.com/science/article/pii/S002251931830599X
36. Langlands, A.J., Almet, A.A., Appleton, P.L., Newton, I.P., Osborne, J.M., Näthke, I.S.: Paneth Cell-Rich Regions Separated by a Cluster of Lgr5+ Cells Initiate Crypt Fission in the Intestinal Stem Cell Niche. PLoS Biology **14**(6), 1–31 (2016). DOI 10.1371/journal.pbio.1002491
37. Lasiecka, I.: Unified theory for abstract parabolic boundary problems–a semigroup approach. Applied Mathematics and Optimization **6**(1), 287–333 (1980)
38. Litvak, Y., Byndloss, M.X., Bäumler, A.J.: Colonocyte metabolism shapes the gut microbiota. Science **362**(6418), eaat9076 (2018). DOI 10.1126/science.aat9076. URL http://www.sciencemag.org/lookup/doi/10.1126/science.aat9076
39. Lopez-Garcia, C., Klein, A.M., Simons, B.D., Winton, D.J.: Intestinal stem cell replacement follows a pattern of neutral drift. Science **330**(6005), 822–825 (2010). DOI 10.1126/science.1196236
40. Lushnikov, P.M., Chen, N., Alber, M.: Macroscopic dynamics of biological cells interacting via chemotaxis and direct contact. Physical Review E **78**(6), 061904 (2008)

41. Martin-Gallausiaux, C., Marinelli, L., Blottière, H.M., Larraufie, P., Lapaque, N.: Scfa: mechanisms and functional importance in the gut. Proceedings of the Nutrition Society **80**(1), 37–49 (2020). DOI 10.1017/s0029665120006916
42. McMurtrey, R.J.: Analytic Models of Oxygen and Nutrient Diffusion, Metabolism Dynamics, and Architecture Optimization in Three-Dimensional Tissue Constructs with Applications and Insights in Cerebral Organoids. Tissue Engineering Part C: Methods **22**(3), 221–249 (2016). DOI 10.1089/ten.tec.2015.0375. URL https://www.liebertpub.com/doi/10.1089/ten.tec.2015.0375
43. Moorthy, A.S., Brooks, S.P., Kalmokoff, M., Eberl, H.J.: A spatially continuous model of carbohydrate digestion and transport processes in the colon. PloS one **10**(12), e0145309 (2015)
44. Morris, M.D.: Factorial Sampling Plans for Preliminary Computational Experiments. Technometrics **33**(2), 161–174 (1991). DOI 10.1080/00401706.1991.10484804. URL http://www.tandfonline.com/doi/abs/10.1080/00401706.1991.10484804
45. Murray, P.J., Edwards, C.M., Tindall, M.J., Maini, P.K.: From a discrete to a continuum model of cell dynamics in one dimension. Physical Review E **80**(3), 031912 (2009)
46. Murray, P.J., Walter, A., Fletcher, A.G., Edwards, C.M., Tindall, M.J., Maini, P.K.: Comparing a discrete and continuum model of the intestinal crypt. Physical Biology **8**(2), 026011 (2011). DOI 10.1088/1478-3975/8/2/026011. URL https://iopscience.iop.org/article/10.1088/1478-3975/8/2/026011
47. Muñoz-Tamayo, R., Laroche, B., Éric Walter, Doré, J., Leclerc, M.: Mathematical modelling of carbohydrate degradation by human colonic microbiota. Journal of Theoretical Biology **266**(1), 189–201 (2010). DOI https://doi.org/10.1016/j.jtbi.2010.05.040. URL https://www.sciencedirect.com/science/article/pii/S0022519310002845
48. Naito, T., Mulet, C., De Castro, C., Molinaro, A., Saffarian, A., Nigro, G., Bérard, M., Clerc, M., Pedersen, A.B., Sansonetti, P.J., Pédron, T.: Lipopolysaccharide from crypt-specific core microbiota modulates the colonic epithelial proliferation-to-differentiation balance. mBio **8**(5), 1–16 (2017). DOI 10.1128/mBio.01680-17
49. Neumann, P.A., Koch, S., Hilgarth, R.S., Perez-Chanona, E., Denning, P., Jobin, C., Nusrat, A.: Gut commensal bacteria and regional Wnt gene expression in the proximal versus distal colon. American Journal of Pathology **184**(3), 592–599 (2014). DOI 10.1016/j.ajpath.2013.11.029. URL http://dx.doi.org/10.1016/j.ajpath.2013.11.029
50. Park, J.H., Kotani, T., Konno, T., Setiawan, J., Kitamura, Y., Imada, S., Usui, Y., Hatano, N., Shinohara, M., Saito, Y., Murata, Y., Matozaki, T.: Promotion of intestinal epithelial cell turnover by commensal bacteria: Role of short-chain fatty acids. PLoS ONE **11**(5), 1–22 (2016). DOI 10.1371/journal.pone.0156334
51. Pearce, S.C., Weber, G.J., van Sambeek, D.M., Soares, J.W., Racicot, K., Breault, D.T.: Intestinal enteroids recapitulate the effects of short-chain fatty acids on the intestinal epithelium. PLOS ONE **15**(4), e0230231 (2020). DOI 10.1371/journal.pone.0230231. URL http://dx.doi.org/10.1371/journal.pone.0230231https://dx.plos.org/10.1371/journal.pone.0230231
52. Pianosi, F., Sarrazin, F., Wagener, T.: A Matlab toolbox for Global Sensitivity Analysis. Environmental Modelling & Software **70**, 80–85 (2015). DOI 10.1016/j.envsoft.2015.04.009. URL https://www.sciencedirect.com/science/article/pii/S1364815215001188
53. Purcell, E.M.: Life at low Reynolds number. American Journal of Physics **45**(1), 3–11 (1977). DOI 10.1119/1.10903. URL http://aapt.scitation.org/doi/10.1119/1.10903
54. Rivera-Chávez, F., Lopez, C.A., Bäumler, A.J.: Oxygen as a driver of gut dysbiosis. Free Radical Biology and Medicine **105**, 93–101 (2017). DOI 10.1016/j.freeradbiomed.2016.09.022. URL https://linkinghub.elsevier.com/retrieve/pii/S0891584916304361. ****
55. Ryu, S.H., Kaiko, G.E., Stappenbeck, T.S.: Cellular differentiation: Potential insight into butyrate paradox? Molecular & Cellular Oncology **5**(3), e1212685 (2018). DOI 10.1080/23723556.2016.1212685. URL https://doi.org/10.1080/23723556.2016.1212685
56. Saltelli, A., Aleksankina, K., Becker, W., Fennell, P., Ferretti, F., Holst, N., Li, S., Wu, Q.: Why so many published sensitivity analyses are false: A systematic review of sensitivity analysis practices. Environmental Modelling & Software **114**, 29–39 (2019). DOI 10.1016/j.envsoft.2019.01.012. URL https://linkinghub.elsevier.com/retrieve/pii/S1364815218302822
57. Sancho, R., Cremona, C.A., Behrens, A.: Stem cell and progenitor fate in the mammalian intestine: Notch and lateral inhibition in homeostasis and disease. EMBO reports **16**(5), 571–81 (2015). DOI 10.15252/embr.201540188. URL http://embor.embopress.org/content/16/5/571.abstract
58. Sarrazin, F., Pianosi, F., Wagener, T.: Global Sensitivity Analysis of environmental models: Convergence and validation. Environmental Modelling & Software **79**, 135–152 (2016). DOI

10.1016/j.envsoft.2016.02.005. URL https://www.sciencedirect.com/science/article/pii/S1364815216300251

59. Sasaki, N., Sachs, N., Wiebrands, K., Elenbroek, S.I.J., Fumagalli, A., Lyubimova, A., Begthel, H., van den Born, M., van Es, J.H., Karthaus, W.R., Li, V.S.W., López-Iglesias, C., Peters, P.J., van Rheenen, J., van Oudenaarden, A., Clevers, H.: Reg4+ deep crypt secretory cells function as epithelial niche for Lgr5+ stem cells in colon. Proceedings of the National Academy of Sciences **113**(37), E5399–E5407 (2016). DOI 10.1073/PNAS.1607327113. URL http://www.pnas.org/content/113/37/E5399
60. Sengupta, S., Muir, J.G., Gibson, P.R.: Does butyrate protect from colorectal cancer? Journal of Gastroenterology and Hepatology **21**(1), 209–218 (2006). DOI 10.1111/j.1440-1746.2006.04213.x
61. Serra, D., Mayr, U., Boni, A., Lukonin, I., Rempfler, M., Challet Meylan, L., Stadler, M.B., Strnad, P., Papasaikas, P., Vischi, D., Waldt, A., Roma, G., Liberali, P.: Self-organization and symmetry breaking in intestinal organoid development. Nature **569**(7754), 66–72 (2019). DOI 10.1038/s41586-019-1146-y. URL http://www.nature.com/articles/s41586-019-1146-y
62. Shyer, A.E., Tallinen, T., Nerurkar, N.L., Wei, Z., Gil, E.S., Kaplan, D.L., Tabin, C.J., Mahadevan, L.: Villification: How the gut gets its villi. Science **342**(6155), 212–218 (2013). DOI 10.1126/science.1238842
63. Snippert, H.J.: Colonic Crypts: Safe Haven from Microbial Products. Cell **165**(7), 1564–1566 (2016). DOI 10.1016/j.cell.2016.06.003. URL https://linkinghub.elsevier.com/retrieve/pii/S0092867416307322. *
64. Snippert, H.J., van der Flier, L.G., Sato, T., van Es, J.H., van den Born, M., Kroon-Veenboer, C., Barker, N., Klein, A.M., van Rheenen, J., Simons, B.D., Clevers, H.: Intestinal crypt homeostasis results from neutral competition between symmetrically dividing Lgr5 stem cells. Cell **143**(1), 134–144 (2010). DOI 10.1016/j.cell.2010.09.016. URL http://dx.doi.org/10.1016/j.cell.2010.09.016
65. Sunter, J.P., Appleton, D.R., de Rodriguez, M.S., Wright, N.A., Watson, A.J.: A comparison of cell proliferation at different sites within the large bowel of the mouse. Journal of Anatomy **129**(4), 833–842 (1979)
66. Tetteh, P.W., Basak, O., Farin, H.F., Wiebrands, K., Kretzschmar, K., Begthel, H., Van Den Born, M., Korving, J., De Sauvage, F., Van Es, J.H., Van Oudenaarden, A., Clevers, H.: Replacement of Lost Lgr5-Positive Stem Cells through Plasticity of Their Enterocyte-Lineage Daughters. Cell Stem Cell **18**(2), 203–213 (2016). DOI 10.1016/j.stem.2016.01.001. URL http://dx.doi.org/10.1016/j.stem.2016.01.001
67. Thalheim, T., Quaas, M., Herberg, M., Braumann, U.D., Kerner, C., Loeffler, M., Aust, G., Galle, J.: Linking stem cell function and growth pattern of intestinal organoids. Developmental Biology **433**(September 2017), 254–261 (2017). DOI 10.1016/j.ydbio.2017.10.013
68. Tomas, J., Reygner, J., Mayeur, C., Ducroc, R., Bouet, S., Bridonneau, C., Cavin, J.B., Thomas, M., Langella, P., Cherbuy, C.: Early colonizing Escherichia coli elicits remodeling of rat colonic epithelium shifting toward a new homeostatic state. ISME Journal **9**(1), 46–58 (2015). DOI 10.1038/ismej.2014.111. URL http://dx.doi.org/10.1038/ismej.2014.111
69. Tóth, B., Ben-Moshe, S., Gavish, A., Barkai, N., Itzkovitz, S.: Early commitment and robust differentiation in colonic crypts. Molecular Systems Biology **13**(1), 902 (2017). DOI 10.15252/msb.20167283
70. Twarogowska, M.: Numerical approximation and analysis of mathematical models arising in cells movement p. 209 (2011)
71. Wang, Y.: Bioengineered Systems and Designer Matrices That Recapitulate the Intestinal Stem Cell Niche **5**(3), 15 (2018)

A Jump rates definitions

We detail the jump rates used in the model as summed up in Table 1.

A.1 Jump rates for Sect. 4.3 and 4.4

For stem cells:

$$\begin{aligned} q^{\infty}_{div,sc} q_{div,sc}(z,l,\mathbf{d}(\nu,z)) =& \mathbb{1}_{\{l=sc\}} q^{\infty}_{div,sc} \Big(1 - R(z, K_{div,sc}[z], \ell_{div,sc}[z])\Big) \\ & \times \Big(1 - R(\mathbf{d}(\nu,z), K_{div,sc}[dens], \ell_{div,sc}[dens])\Big), \end{aligned} \tag{30}$$

$$q^{\infty}_{sc,pc} q_{sc,pc}(z,l) = \mathbb{1}_{\{l=sc\}} q^{\infty}_{sc,pc} R(z, K_{sc,pc}[z], \ell_{sc,pc}[z]). \tag{31}$$

For progenitor cells:

$$\begin{aligned} q^{\infty}_{div,pc} q_{div,pc}(z,l,\mathbf{d}(\nu,z)) =& \mathbb{1}_{\{l=pc\}} q^{\infty}_{div,pc} \Big(1 - R(z, K_{div,pc}[z], \ell_{div,pc}[z])\Big) \\ & \times \Big(1 - R(\mathbf{d}(\nu,z), K_{div,pc}[dens], \ell_{div,pc}[dens])\Big), \end{aligned} \tag{32}$$

$$q^{\infty}_{pc,ent} q_{pc,ent}(z,l) = \mathbb{1}_{\{l=pc\}} q^{\infty}_{pc,ent} R(z, K_{pc,ent}[z], \ell_{pc,ent}[z]), \tag{33}$$

$$q^{\infty}_{pc,gc} q_{pc,gc}(z,l) = \mathbb{1}_{\{l=pc\}} q^{\infty}_{pc,gc} R(z, K_{pc,gc}[z], \ell_{pc,gc}[z]). \tag{34}$$

For enterocytes:

$$\begin{aligned} q^{\infty}_{ex,ent} q_{ex,ent}(z,l,\mathbf{d}(\nu,z)) = \mathbb{1}_{\{l=ent\}} & q^{\infty}_{ex,ent} R(z, K_{ex,ent}[z], \ell_{ex,ent}[z]) \\ & \times R(\mathbf{d}(\nu,z), K_{ex,ent}[dens], \ell_{ex,ent}[dens]). \end{aligned} \tag{35}$$

For goblet cells:

$$q^{\infty}_{ex,gc} q_{ex,gc}(z,l,\mathbf{d}(\nu,z)) = \mathbb{1}_{\{l=gc\}} q^{\infty}_{ex,gc} R(z, K_{ex,gc}[z], \ell_{ex,gc}[z]) \times R(\mathbf{d}(\nu,z), K_{ex,gc}[dens], \ell_{ex,gc}[dens]). \tag{36}$$

A.2 Jump rate definition of the complete model

The jump rate dependency to butyrate, space and cell density is the following.

For stem cells:

$$\begin{aligned} q^{\infty}_{div,sc} q_{div,sc}(z,l,\mathbf{d}(\nu,z)) = \mathbb{1}_{\{l=sc\}} & q^{\infty}_{div,sc} \Big(1 - R(z, K_{div,sc}[z], \ell_{div,sc}[z])\Big) \\ & \times \Big(1 - R(\mathbf{d}(\nu,z), K_{div,sc}[dens], \ell_{div,sc}[dens])\Big) \times \Big(1 - R(\mathbf{c_b}(z), K_{div,sc}[but], \ell_{div,sc}[but])\Big), \end{aligned} \tag{37}$$

$$q^{\infty}_{sc,pc} q_{sc,pc}(z,l) = \mathbb{1}_{\{l=sc\}} q^{\infty}_{sc,pc} R(z, K_{sc,pc}[z], \ell_{sc,pc}[z]). \tag{38}$$

For progenitor cells:

$$\begin{aligned} q^{\infty}_{div,pc} q_{div,pc}(z,l,\mathbf{d}(\nu,z)) =& \mathbb{1}_{\{l=pc\}} q^{\infty}_{div,pc} \Big(1 - R(z, K_{div,pc}[z], \ell_{div,pc}[z])\Big) \\ & \times \Big(1 - R(\mathbf{d}(\nu,z), K_{div,pc}[dens], \ell_{div,pc}[dens])\Big), \end{aligned} \tag{39}$$

$$q^{\infty}_{pc,ent} q_{pc,ent}(z,l) = \mathbb{1}_{\{l=pc\}} q^{\infty}_{pc,ent} R(z, K_{pc,ent}[z], \ell_{pc,ent}[z]) \times R(\mathbf{c_b}(z), K_{pc,ent}[but], \ell_{pc,ent}[but]), \tag{40}$$

$$q^{\infty}_{pc,gc} q_{pc,gc}(z,l) = \mathbb{1}_{\{l=pc\}} q^{\infty}_{pc,gc} R(z, K_{pc,gc}[z], \ell_{gc,pc}[z]) \times R(\mathbf{c_b}(z), K_{pc,gc}[but], \ell_{pc,gc}[but]). \tag{41}$$

For enterocytes:

$$\begin{aligned} q^{\infty}_{ex,ent} q_{ex,ent}(z,l,\mathbf{d}(\nu,z)) = \mathbb{1}_{\{l=ent\}} & q^{\infty}_{ex,ent} R(z, K_{ex,ent}[z], \ell_{ex,ent}[z]) \\ & \times R(\nu * D_a(z), K_{ex,ent}[dens], \ell_{ex,ent}[dens]). \end{aligned} \tag{42}$$

For goblet cells:

$$q^{\infty}_{ex,gc} q_{ex,gc}(z,l,\mathbf{d}(\nu,z)) = \mathbb{1}_{\{l=gc\}} q^{\infty}_{ex,gc} R(z, K_{ex,gc}[z], \ell_{ex,gc}[z]) \times R(\mathbf{d}(\nu,z), K_{ex,gc}[dens], \ell_{ex,gc}[dens]). \tag{43}$$

B Existence and regularity of deterministic trajectories

The global existence and C^1 regularity of the ODE part describing cells trajectories comes from the Cauchy-Lipschitz theorem. We briefly sketch existence and regularity results for the PDE part describing concentrations. For the butyrate concentration, the operator $A_1 = \sigma\partial_{zz}$ with domain $\mathscr{D}(A_1) = \{c \in H^2(]0, z_{max}[_a),\ \partial_z c(-a/2) = 0,\ c(z_{max}+a/2) = 0\}$ is a Riesz spectral operator on $]0, z_{max}[_a$, that generates a strongly continuous, analytic semigroup S_1 on $L^2(]0, z_{max}[_a)$ (see e.g. [21]). For the oxygen concentration, the same holds for $A_2 = \sigma\partial_{zz}$ with domain $\mathscr{D}(A_2) = \{c \in H^2(]0, z_{max}[_a),\ c(-a/2) = 0,\ \partial_z c(z_{max}+a/2) = 0\}$, with associated semigroup S_2. It fits the framework proposed in [37], so that setting

$$W^{2,1}_{L^2(]0,z_{max}[_a)} = \left\{ f \in L^2([0,T], H^2(]0, z_{max}[_a));\ \frac{\partial f}{\partial t} \in L^2([0,T], L^2(]0, z_{max}[_a) \right\}$$

where $H^\alpha(]0, z_{max}[_a)$ are the standard Sobolev spaces, and denoting $S = (S_1, S_2)$ the semigroup induced on the product space $L^2(]0, z_{max}[_a)^2$, the following property holds:

Proposition 1 *Let $c_0 = (c_{01}, c_{02}) \in H^1(]0, z_{max}[_a)^2$, $(c_{lum}, c_{bot}) \in \left(H^1[0,T]\right)^2$ and $u = (u_1, u_2) \in \left(L^2([0,T], L^2(]0, z_{max}[_a))\right)^2$, such that $c_{01}(z_{max}+a/2) = c_{lum}(0)$ and $c_{02}(-a/2) = c_{bot}(0)$, then the evolution problem*

$$\begin{aligned} &\partial_t c_i - \sigma\Delta c_i = u_i, \text{ for i=1,2} \\ &\partial_z c_1(-a/2, t) = 0, \quad c_2(-a/2, t) = c_{bot}, \\ &c_1(z_{max}+a/2, t) = c_{lum}, \quad \partial_z c_2(z_{max}+a/2, t) = 0, \\ &c(\cdot, 0) = c_0 \end{aligned} \tag{44}$$

admits a unique weak solution in $\left(W^{2,1}_{L^2(]0,z_{max}[_a)} \cap C([0,T], H^1(]0, z_{max}[_a))\right)^2$ given by

$$\begin{aligned} c(z,t) = (\mathbb{1}_{]0,z_{max}[_a}(z)c_{lum}(t), \mathbb{1}_{]0,z_{max}[_a}(z)c_{bot}(t)) + S(t)(c_0 - (\mathbb{1}_{]0,z_{max}[_a}(z)c_{lum}(0), \mathbb{1}_{]0,z_{max}[_a}(z)c_{bot}(0))) \\ - \int_0^t S(t-s)(\mathbb{1}_{]0,z_{max}[_a}(z)\frac{dc_{lum}}{dt}(s), \mathbb{1}_{]0,z_{max}[_a}(z)\frac{dc_{bot}}{dt}(s))ds + \\ \int_0^t S(t-s)u(z,s)ds. \end{aligned}$$

Now the semilinear PDEs (6) can be viewed as (44) with u replaced by a nonlinear perturbation taking the form of an operator defined on $L^2(]0, z_{max}[_a)^2 \times [0,T]$ by

$$F(c,t) = (-4\gamma^\infty \frac{c_o^4 c_b}{c_o^4 c_b + K_\beta} \times (\nu_t^{gc} + \nu_t^{ent}) * \psi_a(z), -\gamma^\infty \frac{c_o^4 c_b}{c_o^4 c_b + K_\beta} \times (\nu_t^{gc} + \nu_t^{ent}) * \psi_a(z))$$

This operator is locally Lipschitz in c on $L^2(]0, z_{max}[_a)^2$, uniformly in t on $[0,T]$, when ν_t is a fixed, measurable function from $[0,T]$ to $\mathscr{M}_{F^+}(\mathscr{X})$ endowed with the weak convergence topology and the associated Borel σ-algebra, such that $\sup_{t\le T}\langle \nu_t, 1\rangle < \infty$. Using proposition 1, together with a standard fixed point argument we obtain the local existence (in time) of the solutions of PDEs (6), that can be extended to a global existence on $[0,T]$. More precisely,

Proposition 2 *Let ν_t as above, and $c_0 = (c_{01}, c_{02}) \in H^1(]0, z_{max}[_a)^2$, $(c_{lum}, c_{bot}) \in \left(H^1[0,T]\right)^2$ such that $c_{01}(z_{max}+a/2) = c_{lum}(0)$ and $c_{02}(-a/2) = c_{bot}(0)$. The non-linear evolution problem* (6) *admits a unique solution c in $\left(W^{2,1}_{L^2(]0,z_{max}[_a)} \cap C([0,T], H^1(]0, z_{max}[_a))\right)^2$.*

C PDMP stability

We aim at showing that an almost finite number of jump occurs during any finite time interval. We first introduce the independent Poisson probability measures $N_k(d\theta, i, dt)$ associated to each jump type $k \in \mathscr{E}$, defined on $[0,1] \times \mathbb{N}^* \times \mathbb{R}_+$ with intensity

$$n_k(d\theta, i, dt) = q_k^\infty d\theta dt \sum_{k\in\mathbb{N}} \delta_k(i). \tag{45}$$

The process introduced in Sect. 2 is solution of the following SDE, which is called the pathwise representation of the process

$$(c_t,\nu_t) = A_t(c_0,\nu_0) + \sum_{k\in\mathscr{E}} \int_0^t \int_{\mathbb{N}^*} \int_0^1 \left[A_{t-s}(c_s,\nu_{s^-}+\mu_k(x^i_{s^-}))) - A_{t-s}(c_s,\nu_{s^-})\right] \mathbb{1}_{\{i\leq\langle\nu_{s^-},1\rangle\}}(i)\mathbb{1}_{\{\theta\leq q_k(x^i_{s^-},\nu_{s^-}*D_k(x^i_{s^-}),c_s*\psi_a(z^i_{s^-}))\}}(\theta)N_k(d\theta,i,ds). \quad (46)$$

Fig.15 sketches the rationale behind this formula, built upon the remark that if T_n and T_{n-1} are successive jump times, then for $t > T_n$,

$$A_{t-T_{n-1}}(c_{T_{n-1}},\nu_{T_{n-1}}) = A_{t-T_n}(c_{T_n},\nu_{T_n^-}).$$

Note that, when possible without ambiguity, we simplify the notation $\mathbb{1}_{\{\theta\leq q_k(x^i_{s^-},\nu_{s^-}*D_k(x^i_{s^-}),c_s*\psi_a(z^i_{s^-}))\}}(\theta)$ by $\mathbb{1}_{\{\theta\leq q_k(\cdot)\}}(\theta)$.

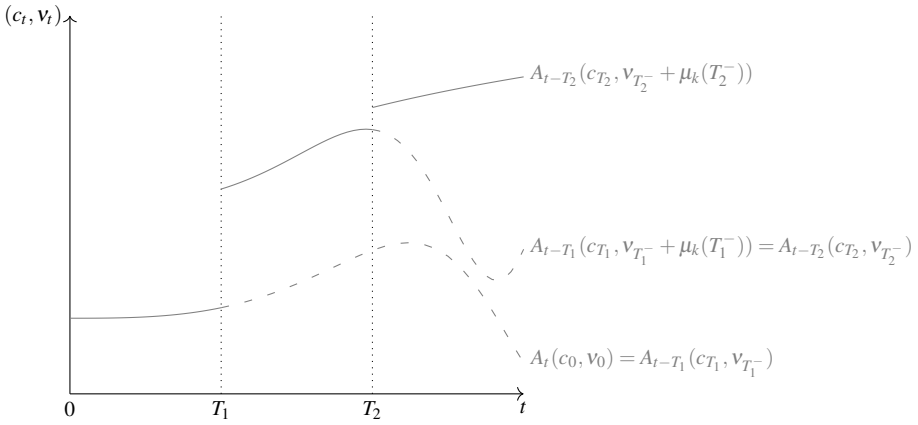

Fig. 15: **Sketch of the process trajectory.** The trajectory $A_t(c_0,\nu_0)$ is first plotted. After the first jump, the trajectory $A_t(c_0,\nu_0)$ for $t \geq T_1$, which equals $A_{t-T_1}(c_{T_1},\nu_{T_1^-})$, is replaced by $A_{t-T_1}(c_{T_1},\nu_{T_1^-}+\mu_k(T_1^-))$. This process is iterated at each jump.

For all $n \in \mathbb{N}$, we define the stopping time $\tau_n = \inf\{t \geq 0, \langle\nu_t,1\rangle = n\}$. Let

$$T_n(t) := \min(t,\tau_n). \quad (47)$$

The stopped process at n cells is $(c_{T_n(t)},\nu_{T_n(t)})_{t\geq 0}$. $\mathscr{C}^{p,q,\bullet}(\mathbb{R}^+\times\mathscr{X},\mathbb{R})$ denotes the space of functions $f(t,z,l)$ that are p times derivable with respect to t and q times derivable with respect to z for all $l \in \mathscr{T}$.

Lemma C1 *Let $f \in \mathscr{C}^{1,1,\bullet}(\mathbb{R}^+ \times \mathscr{X}, \mathbb{R})$, $g \in H^1(]0, z_{max}[_a)^2$, $\psi \in \mathscr{C}^1(\mathbb{R}^2)$, $t \in \mathbb{R}$. We denote by $\langle c, g\rangle_{L^2}$ the scalar product in L^2. Then, for $t > 0$ and $n \geq \langle \nu_0, 1\rangle$,*

$$\begin{aligned}
\psi(\langle c_{T_n(t)}, g\rangle_{L^2}, \langle \nu_{T_n(t)}, f_{T_n(t)}\rangle) &= \psi(\langle c_0, g\rangle, \langle \nu_0, f_0\rangle) \\
&\quad + \int_0^t \partial_1 \psi(\langle c_s, g\rangle_{L^2}, \langle \nu_s, f_s\rangle) \langle \partial_s c_s, g\rangle_{L^2} \mathbb{1}_{\{s \leq T_n(t)\}}(s)\, ds \\
&\quad + \int_0^t \partial_2 \psi(\langle c_s, g\rangle_{L^2}, \langle \nu_s, f_s\rangle) \langle \nu_s, \phi \nu_s * F_a \nabla_z f_s + \partial_s f_s\rangle \mathbb{1}_{\{s \leq T_n(t)\}}(s)\, ds \\
&\quad + \sum_{k \in \mathscr{E}} \int_0^t \int_{\mathbb{N}^*} \int_0^1 \big[\psi(\langle c_s, g\rangle_{L^2}, \langle \nu_{s^-} + \mu_k(x^i_{s^-}), f_s\rangle) - \psi(\langle c_s, g\rangle_{L^2}, \langle \nu_{s^-}, f_s\rangle)\big] \\
&\qquad \times \mathbb{1}_{\{s \leq T_n(t)\}} \mathbb{1}_{\{i \leq \langle \nu_{s^-}, 1\rangle\}} \mathbb{1}_{\{\theta \leq q_k(\cdot)\}} N_k(d\theta, di, ds). \qquad (48)
\end{aligned}$$

Proof Using the pathwise representation of the PDMP (46), we get

$$\begin{aligned}
\langle \nu_{T_n(t)}, f_{T_n(t)}\rangle &= \langle \tilde{A}_{T_n(t)}(c_0, \nu_0), f_{T_n(t)}\rangle \\
&\quad + \sum_{k \in \mathscr{E}} \int_0^{T_n(t)} \int_{\mathbb{N}^*} \int_0^1 \big[\langle \tilde{A}_{T_n(t)-s}(c_s, \nu_{s^-} + \mu_k(x^i_{s^-})), f_{T_n(t)}\rangle - \langle \tilde{A}_{T_n(t)-s}(c_s, \nu_{s^-}), f_{T_n(t)}\rangle\big] \\
&\qquad \times \mathbb{1}_{\{i \leq \langle \nu_{s^-}, 1\rangle\}} \mathbb{1}_{\{\theta \leq q_k(\cdot)\}} N_k(d\theta, di, ds)
\end{aligned}$$

where the stochastic integral is correctly defined since the population size is majored by n, and f is continuous on the compact $\mathscr{X}$.

Then, applying formula (12) , the first term of the RHS can be written

$$\langle \tilde{A}_{T_n(t)}(c_0, \nu_0), f_{T_n(t)}\rangle = \langle \nu_0, f_0\rangle + \int_0^{T_n(t)} \langle \tilde{A}_u(c_0, \nu_0), \phi \tilde{A}_u(c_0, \nu_0) * F_a \nabla_z f_u + \partial_u f_u\rangle du,$$

and the second one

$$\begin{aligned}
&\sum_{k \in \mathscr{E}} \int_0^{T_n(t)} \int_{\mathbb{N}^*} \int_0^1 \big(\langle \nu_{s^-} + \mu_k(x^i_{s^-}), f_s\rangle - \langle \nu_{s^-}, f_s\rangle\big) \\
&\qquad \times \mathbb{1}_{\{i \leq \langle \nu_{s^-}, 1\rangle\}} \mathbb{1}_{\{\theta \leq q_k(\cdot)\}} N_k(d\theta, di, ds) \\
&\quad + \sum_{k \in \mathscr{E}} \int_0^{T_n(t)} \int_{\mathbb{N}^*} \int_0^1 \int_s^{T_n(t)} \big[\langle \tilde{A}_{u-s}(c_s, \nu_{s^-} + \mu_k(x^i_{s^-})), \phi \tilde{A}_{u-s}(c_s, \nu_{s^-} + \mu_k(x^i_{s^-})) * F_a \nabla_z f_u + \partial_u f_u\rangle \\
&\qquad - \langle \tilde{A}_{u-s}(c_s, \nu_{s^-}), \phi \tilde{A}_{u-s}(c_s, \nu_{s^-}) * F_a \nabla_z f_u + \partial_u f_u\rangle\big] \\
&\qquad \times \mathbb{1}_{\{i \leq \langle \nu_{s^-}, 1\rangle\}} \mathbb{1}_{\{\theta \leq q_k(\cdot)\}}\, du N_k(d\theta, di, ds).
\end{aligned}$$

Due to the smoothness of f, $\partial_t f$ and $\nabla_z f$, Fubini's theorem and formula (46) are applied to the last integral term to get:

$$\begin{aligned}
&\int_0^{T_n(t)} \sum_{k \in \mathscr{E}} \int_0^u \int_{\mathbb{N}^*} \int_0^1 \big[\langle \tilde{A}_{u-s}(c_s, \nu_{s^-} + \mu_k(x^i_{s^-})), \phi \tilde{A}_{u-s}(c_s, \nu_{s^-} + \mu_k(x^i_{s^-})) * F_a \nabla_z f_u + \partial_u f_u\rangle \\
&\qquad - \langle \tilde{A}_{u-s}(c_s, \nu_{s^-}), \phi \tilde{A}_{u-s}(c_s, \nu_{s^-}) * F_a \nabla_z f_u + \partial_u f_u\rangle\big] \\
&\qquad \times \mathbb{1}_{\{i \leq \langle \nu_{s^-}, 1\rangle\}} \mathbb{1}_{\{\theta \leq q_k(\cdot)/q_k^\infty\}} N_k(d\theta, di, ds) du \\
&= \int_0^{T_n(t)} \langle \nu_u, \phi \nu_u * F_a \nabla_z f_u + \partial_u f_u\rangle - \langle \tilde{A}_u(c_0, \nu_0), \phi \tilde{A}_u(c_0, \nu_0) * F_a \nabla_z f_u + \partial_u f_u\rangle\, du.
\end{aligned}$$

We then have:

$$\begin{aligned}
\langle \nu_{T_n(t)}, f_{T_n(t)} \rangle &= \langle \nu_0, f_0 \rangle + \int_0^{T_n(t)} \langle \tilde{A}_u(c_0,\nu_0), \phi\tilde{A}_u(c_0,\nu_0) * F_a \nabla_z f_u + \partial_u f_u \rangle du \\
&+ \int_0^{T_n(t)} \langle \nu_u, \phi\nu_u * F_a\nabla_z f_u + \partial_u f_u \rangle - \int_0^{T_n(t)} \langle \tilde{A}_u(c_0,\nu_0), \phi\tilde{A}_u(c_0,\nu_0) * F_a\nabla_z f_u + \partial_u f_u \rangle \, du \\
&+ \sum_{k\in\mathscr{E}} \int_0^{T_n(t)} \int_{\mathbb{N}^*} \int_0^1 \left(\langle \nu_{s^-} + \mu_k(x^i_{s^-}), f_s \rangle - \langle \nu_{s^-}, f_s \rangle \right) \mathbb{1}_{\{i \le \langle \nu_{s^-},1\rangle\}} \mathbb{1}_{\{\theta \le q_k(\cdot)\}} \, N_k(d\theta, di, ds) \\
&= \langle \nu_0, f_0 \rangle + \int_0^t \langle \nu_u, \phi\nu_u * F_a\nabla_z f_u + \partial_u f_u \rangle \mathbb{1}_{\{u \le T_n(t)\}} \, du \\
&+ \sum_{k\in\mathscr{E}} \int_0^t \int_{\mathbb{N}^*} \int_0^1 \langle \mu_k(x^i_{s^-}), f_s \rangle \mathbb{1}_{\{s\le T_n(t)\}} \mathbb{1}_{\{i \le \langle \nu_{s^-},1\rangle\}} \mathbb{1}_{\{\theta \le q_k(\cdot)\}} \, N_k(d\theta, di, ds).
\end{aligned}$$

We also have

$$\langle c_{T_n(t)}, g \rangle_{L^2} = \langle c_0, g \rangle + \int_0^t \langle \partial_s c_s, g \rangle_{L^2} \mathbb{1}_{\{s \le T_n(t)\}} \, ds.$$

Then, multidimensional Itô's formula with jumps is applied to get the desired expression.

We now have a tool to study the stability of the PDMP. We must show that the population does not explode in finite time.

Lemma C2 *For any $t \ge 0$, if an integer $p \ge 1$ such that $\mathbb{E}[\langle \nu_0, 1\rangle^p] < \infty$ exists then*

$$\mathbb{E}\left[\sup_{s \le t} \langle \nu_s, 1 \rangle^p \right] \le C(p,t) \tag{49}$$

where $C(p,t) < \infty$ is a constant that only depends on p and t.

Proof For all $n \in \mathbb{N}$, let $T_n(t)$ be as defined in (47). As the deterministic evolution does not impact the population size and the stochastic events modify it with at most one individual by jump, formula (48) applied to $\langle \nu_{T_n(t)}, 1\rangle^p$ gives

$$\begin{aligned}
\langle \nu_{T_n(t)}, 1 \rangle^p =& \langle \nu_0, 1 \rangle^p \\
&+ \sum_{k\in\mathscr{E}} \int_0^{T_n(t)} \int_{\mathbb{N}^*} \int_0^1 \left(\langle \nu_{s^-} + \mu_k(x^i_{s^-}), 1 \rangle^p - \langle \nu_{s^-}, 1\rangle^p \right) \mathbb{1}_{\{i \le \langle \nu_{s^-},1\rangle\}}(i) \\
&\qquad \mathbb{1}_{\{\theta \le q_k(\cdot)\}}(\theta) \, N_k(d\theta, di, ds) \qquad (50) \\
\le \langle \nu_0, 1 \rangle^p &+ \sum_{k\in\mathscr{E}} \int_0^{T_n(t)} \int_{\mathbb{N}^*} \int_0^1 \left[(\langle \nu_{s^-}, 1\rangle + 1)^p - \langle \nu_{s^-}, 1\rangle^p \right] \mathbb{1}_{\{i \le \langle \nu_{s^-},1\rangle\}}(i) \\
&\qquad \mathbb{1}_{\{\theta \le q_k(\cdot)\}}(\theta) \, N_k(d\theta, di, ds). \qquad (51)
\end{aligned}$$

The last integral grows with time since the integrand is non-negative, so that the supremum can be applied in the left hand side. Furthermore, for any non-negative x, $(1+x)^p - x^p \le C(p)(1 + x^{p-1})$. Hence,

$$\begin{aligned}
\sup_{s \le T_n(t)} \langle \nu_s, 1 \rangle^p \le \langle \nu_0, 1 \rangle^p &+ \sum_{k\in\mathscr{E}} \int_0^{T_n(t)} \int_{\mathbb{N}^*} \int_0^1 C(p) \left(\langle \nu_{s^-}, 1\rangle^{p-1} + 1 \right) \mathbb{1}_{\{i \le \langle \nu_{s^-},1\rangle\}}(i) \\
&\qquad \mathbb{1}_{\{\theta \le q_k(\cdot)\}}(\theta) N_k(d\theta, di, ds). \qquad (52)
\end{aligned}$$

Switching to the expectations:

$$\mathbb{E}\left[\sup_{s\leq T_n(t)}\langle \nu_s,1\rangle^p\right] \leq \mathbb{E}[\langle \nu_0,1\rangle^p]$$
$$+\sum_{k\in\mathscr{E}}\mathbb{E}\left[\int_0^{T_n(t)}\int_{\mathbb{N}^*}\int_0^1 C(p)\left(\langle \nu_{s^-},1\rangle^{p-1}+1\right)\mathbb{1}_{\{i\leq\langle \nu_{s^-},1\rangle\}}(i)\mathbb{1}_{\{\theta\leq q_k(\cdot)\}}(\theta)q_k^\infty d\theta\left(\sum_{k\geq 1}\delta_k(di)\right)ds\right]$$
$$\leq \mathbb{E}[\langle \nu_0,1\rangle^p]+\sum_{k\in\mathscr{E}}\mathbb{E}\left[\int_0^{T_n(t)}\sum_{i=1}^{\langle \nu_{s^-},1\rangle} C(p)\left(\langle \nu_{s^-},1\rangle^{p-1}+1\right)q_k^\infty q_k(\cdot)\,ds\right]$$
$$\leq \mathbb{E}[\langle \nu_0,1\rangle^p]+\sum_{k\in\mathscr{E}}\mathbb{E}\left[\int_0^t q_k^\infty C(p)\left(\langle \nu_{s\wedge\tau_n},1\rangle^p+\langle \nu_{s\wedge\tau_n},1\rangle\right)ds\right].$$

Recalling that $n+n^p\leq 2n^p$ for all $p\geq 1$, Fubini's theorem leads to

$$\mathbb{E}\left[\sup_{s\leq T_n(t)}\langle \nu_s,1\rangle^p\right] \leq \mathbb{E}[\langle \nu_0,1\rangle^p]+2C(p)\left(\sum_{k\in\mathscr{E}}q_k^\infty\right)\int_0^t\mathbb{E}\left[\sup_{u\leq s\wedge\tau_n}\langle \nu_u,1\rangle^p\right]ds.$$

and Gronwall lemma provides an estimate that does not depend on n:

$$\mathbb{E}\left[\sup_{s\leq T_n(t)}\langle \nu_s,1\rangle^p\right] \leq \mathbb{E}[\langle \nu_0,1\rangle^p]\exp\left(2C(p)\left(\sum_{k\in\mathscr{E}}q_k^\infty\right)t\right)=C(p,t). \tag{53}$$

Hence $\tau_n\to\infty$ a.s. Indeed, suppose that there exists $T>0$ such that, for all $n\in\mathbb{N}$, $\mathbb{P}(\tau_n\leq T)>\varepsilon>0$. We remark that

$$\tau_n\leq T \Rightarrow \sup_{s\leq T_n(T)}\langle \nu_s,1\rangle^p\geq n^p \quad \text{so that} \quad \mathbb{P}(\sup_{s\leq T_n(T)}\langle \nu_s,1\rangle^p\geq n^p)\geq\mathbb{P}(\tau_n\leq T)$$

Hence, by Markov inequality, for all $n\in\mathbb{N}$

$$\mathbb{E}\left[\sup_{s\leq T_n(T)}\langle \nu_s,1\rangle^p\right]\geq\mathbb{P}\left(\sup_{s\leq T_n(T)}\langle \nu_s,1\rangle^p\geq n^p\right)n^p\geq\mathbb{P}(\tau_n\leq T)n^p>\varepsilon n^p$$

which is in contradiction with (53).

Hence, $\lim_{n\to\infty}\sup_{s\leq T_n(t)}\langle \nu_s,1\rangle^p=\sup_{s\leq t}\langle \nu_s,1\rangle^p$ a.s. Fatou's lemma finally gives

$$\mathbb{E}\left[\sup_{s\leq t}\langle \nu_s,1\rangle^p\right]=\mathbb{E}\left[\liminf_{n\to\infty}\sup_{s\leq T_n(t)}\langle \nu_s,1\rangle^p\right]\leq\liminf_{n\to\infty}\mathbb{E}\left[\sup_{s\leq T_n(t)}\langle \nu_s,1\rangle^p\right]\leq C(p,t).$$

The stability of the PDMP is a direct consequence of this lemma.

Corollary C3 *If there exists an integer $p\geq 1$ such that $\mathbb{E}[\langle \nu_0,1\rangle^p]<\infty$, then:*
1. *The PDMP is stable.*
2. *$T_n(t)$ can be replaced by t in formula* (48).

Proof (1): Let $(J_n)_n$ be the sequence of jump times. We aim at showing that $J_n\underset{n\to\infty}{\to}\infty$ a.s. Assume that there exists $T<+\infty$ and a set Ω_T of non-null probability such that, $\forall\,\omega\in\Omega_T$, $\sup_{n\in\mathbb{N}}J_n(\omega)<T$. We recall that, as proven in the proof of Lemma C2, that $\mathbb{E}\left[\sup_{s\leq t}\langle \nu_s,1\rangle\right]<\infty$ implies that $\tau_n\to\infty$ a.s. Hence, it exists $N\in\mathbb{N}$ and a set $\Omega_{T,N}\subset\Omega_T$ of non-null probability such that, $\forall\,\omega\in\Omega_{T,N}$, $T<\tau_N(\omega)$. Let $C(N)$ be an upper bound of the jump rate on $\mathscr{M}_{P^+}(\mathscr{X})_N=\{\nu\in\mathscr{M}_{P^+}(\mathscr{X}),\langle \nu,1\rangle\leq N\}\subset\mathscr{M}_{P^+}(\mathscr{X})$. Such an upper bound exists since the individual jump rates are bounded by q_k^∞ by definition. Hence, for all $\omega\in\Omega_{T,N}$, the jump time sequence $(J_n(\omega))_{n\in\mathbb{N}}$ can be built as an extraction of the sequence $(J'_n(\omega))_{n\in\mathbb{N}}$ of the jump time of a Poisson process with jump rate $C(N)$. But the sequence $(J'_n(\omega))_{n\in\mathbb{N}}$ is a.s. divergent, which comes in contradiction with $\sup_{n\in\mathbb{N}}J_n(\omega)<T$ for all $\omega\in\Omega_T$.

(2): As the stochastic integrals in the proof of Lemma C1 are correctly defined (see e.g. theorem A.3 [7]) due to the hypothesis on ν_0 and Lemma C2.

D A case of bistability

Here we explain the unexpected simulations values we obtained for $K_{div}[dens] = -50\%$ in Sect. 4.2. Starting from an initial number of 700 cells, we see in Fig. 16a that either the number of cells drops below 400 cells and activity in the crypt goes on, or the number of cells stabilises around 500 and the crypt freezes, meaning that no additional extrusion or division events are observed, so that the total cell population does not evolve any longer. We evaluated the fraction of crypt that freezes upon variations of $K_{div}[dens]$, always starting with 700 cells (Fig. 16b). This fraction increases when $K_{div}[dens]$ decreases. Indeed, for low values of $K_{div}[dens]$, cell division is totally inhibited by contact inhibition and the division rate is 0. At first, cells are extruded at the top of the crypt as density of cells (starting from 700 cells) is way above what $K_{div}[dens]$ prescribes. Once exceeding cells have been extruded, the population can reach a mechanical equilibrium where no extrusion occurs at the top of the crypt (as density equilibrium has been reached). Meanwhile, no division occurs in the lower part of the crypt as density is still too high there, and the division rate is therefore zero.

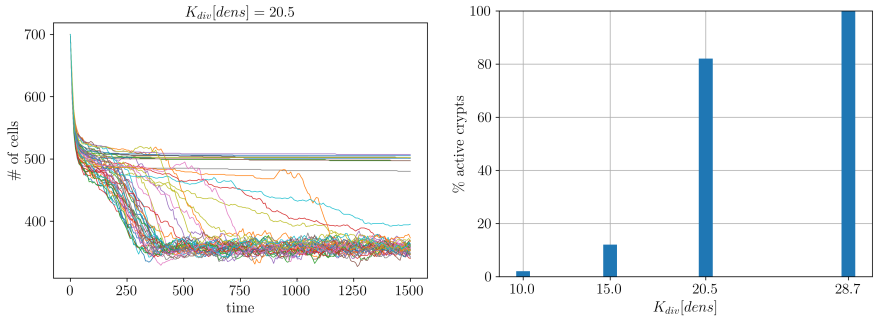

(a) Number of cells

(b) Fraction of active crypts, 50 repetitions

Fig. 16: **Illustration of bistability phenomena for high $K_{div}[dens]$.** We plot the evolution of the total number of cells in 50 repetitions of the model in Sect. 4.2 for $K_{div}[dens] = 20.5$ (left panel). We observe that some simulations show a constant total cell population (around 500 cells) for $t > 250$ without additional stochastic variations, whereas other simulations show stochastic evolution without interruption, but a significantly lower total cell population (around 300 cells). Then, we compute 50 repetitions of the model for different values of $K_{div}[dens]$ and count the fraction of simulations keeping showing stochastic events all along the simulation.

E PDMP parameters values (for the simplified sub-models and the complete model)

PDMP model parameters are given for the different sub-models of increasing complexity studied during the PDMP exploration. Namely, the parameters used for the model with the sole deterministic part, studied in Sect. 4.1, are given in Table 7. When the spatialized division and extrusion events are added in Sect. 4.2, parameters of Table 8 are used. In Sect. 4.3 where cell types are introduced, parameters of Table 9 are used. Adding O_2 and butyrate in Sect. 4.4, we use parameters presented in Table 10. Finally, the complete model including the feedback of butyrate on stem cell division as studied in Sect. 4.5 is implemented with the parameters presented in Table 11.

Table 7: Parameters for Sect. 4.1

	Value	Unit	Description	Ref
z_{max}	200	μm		-
r_0	25	μm		-
ε	$= 0.1 \times r_0$	μm		-
a	10	μm		-
k_a	15	$\mu m \times h^{-1}$		-
d_a	1	$\emptyset$		-

Table 8: Parameters for Sect. 4.2

	Value	Unit	Description	Ref
z_{max}	200	μm		-
r_0	25	μm		-
ε	$= 0.1 \times r_0$	μm		-
a	10	μm		-
k_a	15	$\mu m \times h^{-1}$		-
d_a	1	$\emptyset$		-
q^{∞}_{div}	0.22	h^{-1}		
$K_{div}[z]$	40	μm		
$\ell_{div}[z]$	15	μm		
$K_{div}[dens]$	40	$cell$		
$\ell_{div}[dens]$	6	$cell$		
q^{∞}_{ex}	0.34	h^{-1}		
$K_{ex}[z]$	190	μm		
$\ell_{ex}[z]$	15	μm		

E.1 Parameters of chemical kinetic

We could not find value for the molar concentration of oxygen. Therefore, we switched to normalized concentrations. We set $\bar{c_o} = \frac{c_o}{C}$ with C a normalizing constant. The evolution equation of oxygen concentration 6 becomes

$$\partial_t \bar{c}_o - \sigma_i \partial_{zz} \bar{c}_o = -\frac{s_o}{C} \gamma^{\infty}_{\beta} \frac{\bar{c_o}^4 c_b}{\bar{c_o}^4 c_b + \frac{K^5_{\beta}}{C^4}} (\nu^{ent}_t + \nu^{gc}_t) * \psi_a(z). \tag{54}$$

We suppose that experimental measures of the reaction speed in [19] are done at a standard (normoxic) oxygen concentration c^*_o. The half of the maximal reaction speed is reached experimentally at a butyrate concentration of $0.184\ mole/L$. Therefore,

$$K^5_{\beta} = 0.184 \times c^{*4}_o.$$

We suppose as well that oxygen concentration at the bottom of the crypt is c^*_o. The exact value of c^*_o is unknown to us, but we set $\bar{c}^*_o = 10$. Then, $C = \frac{c^*_o}{\bar{c}^*_o} = \frac{c^*_o}{10}$. Therefore, we can find a value for the parameter K^5_{β}/C^4 of (54):

$$\frac{K^5_{\beta}}{C^4} = \frac{0.184 \times c^{*4}_o \times 10^4}{c^{4*}_o} = 0.184 \times 10^4.$$

As C is unknown, the parameter s_o/C is still unknown, but we decided to use $C = 1$ in all simulations.

F Parameters for the deterministic PDE approximation of the PDMP

Table 9: Parameters for section 4.3

	Value	Unit	Description	Ref
z_{max}	200	μm		-
r_0	25	μm		-
ε	$= 0.1 \times r_0$	μm		-
a	10	μm		-
k_a	15	$\mu m \times h^{-1}$		-
d_a	1	$\emptyset$		-
$q^{\infty}_{div,sc}$	0.09	h^{-1}		-
N_{dcs}	12	$cell$	number of DCS cells	
$\rho_{dcs}(z)dz$	see (25)		spatial distribution of DCS cells	
$K_{div,sc}[z]$	12	μm		-
$\ell_{div,sc}[z]$	5	μm		-
$K_{div,sc}[dens]$	53	$cell$		-
$\ell_{div,sc}[dens]$	6	$cell$		
$q^{\infty}_{sc,pc}$	0.2	h^{-1}		-
$K_{sc,pc}[z]$	$= K_{div,sc}[z]$	μm	-	
$\ell_{sc,pc}[z]$	$= \ell_{div,sc}[z]$	μm	-	
$q^{\infty}_{div,pc}$	0.22	h^{-1}		-
$K_{div,pc}[z]$	40	μm		-
$\ell_{div,pc}[z]$	40	μm		-
$K_{div,pc}[dens]$	41	$cell$		-
$\ell_{div,pc}[dens]$	$= \ell_{div,sc}[dens]$	$cell$		-
$q^{\infty}_{pc,ent}$	0.15	h^{-1}		-
$K_{pc,ent}[z]$	$= K_{div,pc}[z]$	μm		-
$\ell_{pc,ent}[z]$	15	μm		
$q^{\infty}_{pc,gc}$	$= 0.33 \times q^{\infty}_{pc,ent}$	h^{-1}		-
$K_{pc,gc}[z]$	$= K_{pc,ent}[z]$	μm		-
$\ell_{pc,gc}[z]$	$= \ell_{pc,ent}[z]$	μm		-
$q^{\infty}_{ex,ent}$	0.34	h^{-1}		
$K_{ex,ent}[z]$	190	μm		
$\ell_{ex,ent}[z]$	15	μm		
$K_{ex,ent}[dens]$	20	$cell$		
$\ell_{ex,ent}[dens]$	$= \ell_{div,sc}[dens]$	$cell$		
$q^{\infty}_{ex,gc}$	$= q^{\infty}_{ex,ent}$	h^{-1}		
$K_{ex,gc}[z]$	$= K_{ex,ent}[z]$	μm		
$\ell_{ex,gc}[z]$	$= \ell_{ex,ent}[z]$	μm		
$K_{ex,gc}[dens]$	$= K_{ex,ent}[dens]$	$cell$		
$\ell_{ex,gc}[dens]$	$= \ell_{ex,ent}[dens]$	$cell$		

Table 10: Parameters for Sect. 4.4

	Value	Unit	Description	Ref
z_{max}	200	μm		-
r_0	25	μm		-
ε	$= 0.1 \times r_0$	μm		-
a	10	μm		-
k_a	15	$\mu m \times h^{-1}$		-
d_a	1	$\emptyset$		-
N_{dcs}	12	$cell$	number of DCS cells	
$\rho_{dcs}(z)dz$	see (25)		spatial distribution of DCS cells	
$q^{\infty}_{div,sc}$	0.09	h^{-1}		-
$K_{div,sc}[z]$	12	μm		-
$\ell_{div,sc}[z]$	5	μm		-
$K_{div,sc}[dens]$	53	$cell$		-
$\ell_{div,sc}[dens]$	6	$cell$		
$q^{\infty}_{sc,pc}$	0.2	h^{-1}		-
$K_{sc,pc}[z]$	$= K_{div,sc}[z]$	μm	-	
$\ell_{sc,pc}[z]$	$= \ell_{div,sc}[z]$	μm	-	
$q^{\infty}_{div,pc}$	0.22	h^{-1}		-
$K_{div,pc}[z]$	40	μm		-
$\ell_{div,pc}[z]$	40	μm		-
$K_{div,pc}[dens]$	41	$cell$		-
$\ell_{div,pc}[dens]$	$= \ell_{div,sc}[dens]$	$cell$		-
$q^{\infty}_{pc,ent}$	0.15	h^{-1}		-
$K_{pc,ent}[z]$	$= K_{div,pc}[z]$	μm		-
$\ell_{pc,ent}[z]$	15	μm		
$q^{\infty}_{pc,gc}$	$= 0.33 \times q^{\infty}_{pc,ent}$	h^{-1}		-
$K_{pc,gc}[z]$	$= K_{pc,ent}[z]$	μm		-
$\ell_{pc,gc}[z]$	$= \ell_{pc,ent}[z]$	μm		-
$q^{\infty}_{ex,ent}$	0.34	h^{-1}		
$K_{ex,ent}[z]$	190	μm		
$\ell_{ex,ent}[z]$	15	μm		
$K_{ex,ent}[dens]$	20	$cell$		
$\ell_{ex,ent}[dens]$	$= \ell_{div,sc}[dens]$	$cell$		
$q^{\infty}_{ex,gc}$	$= q^{\infty}_{ex,ent}$	h^{-1}		
$K_{ex,gc}[z]$	$= K_{ex,ent}[z]$	μm		
$\ell_{ex,gc}[z]$	$= \ell_{ex,ent}[z]$	μm		
$K_{ex,gc}[dens]$	$= K_{ex,ent}[dens]$	$cell$		
$\ell_{ex,gc}[dens]$	$= \ell_{ex,ent}[dens]$	$cell$		
s_o	-4	$\emptyset$	Stoechiometric coefficient for O_2	-
s_b	-1	$\emptyset$	Stoechiometric coefficient for butyrate	-
σ_o	3.6×10^6	$\mu m^2/h$	Diffusion coefficient for O_2	[42]
σ_{but}	$= \sigma_o$	$\mu m^2/h$	Diffusion coefficient for butyrate	-
γ^{∞}_{β}	1.6×10^4	$10^-15 \times \frac{mmol}{h \times \mu m^2}$	Max. reaction speed of β-oxydation	[18]
K_{β}	$(0.184 \times 10^4)^{1/5}$	mM	Affinity of β-oxydation (supposed experimental normoxic condition)	[19]
$c_{b,lum}$	5	mM	Luminal concentration of butyrate at homeostasis	[32]
$c_{o,bot}$	10	a.u.	Homestatic O_2 concentration at the bottom of the crypt	[54]

Table 11: Parameters for Sect. 4.5.

	Value	Unit	Description	Ref
z_{max}	200	μm		-
r_0	25	μm		-
ε	$= 0.1 \times r_0$	μm		-
a	10	μm		-
k_a	15	$\mu m \times h^{-1}$		-
d_a	1	$\emptyset$		-
N_{dcs}	12	$cell$	number of DCS cells	
$\rho_{dcs}(z)dz$	see (25)		spatial distribution of DCS cells	
$q^{\infty}_{div,sc}$	0.15	h^{-1}		-
$K_{div,sc}[z]$	12	μm		-
$\ell_{div,sc}[z]$	5	μm		-
$K_{div,sc}[dens]$	53	$cell$		-
$\ell_{div,sc}[dens]$	6	$cell$		
$K_{div,sc}[but]$	2			-
$\ell_{div,sc}[but]$	5			
$q^{\infty}_{sc,pc}$	0.2	h^{-1}		-
$K_{sc,pc}[z]$	$= K_{div,sc}[z]$	μm		-
$\ell_{sc,pc}[z]$	$= \ell_{div,sc}[z]$	μm		-
$q^{\infty}_{div,pc}$	0.22	h^{-1}		-
$K_{div,pc}[z]$	40	μm		-
$\ell_{div,pc}[z]$	40	μm		-
$K_{div,pc}[dens]$	41	$cell$		-
$\ell_{div,pc}[dens]$	$= \ell_{div,sc}[dens]$	$cell$		-
$q^{\infty}_{pc,ent}$	0.25	h^{-1}		-
$K_{pc,ent}[z]$	$= K_{div,pc}[z]$	μm		-
$\ell_{pc,ent}[z]$	15	μm		
$K_{pc,ent}[but]$	1.5			
$\ell_{pc,ent}[but]$	5			
$q^{\infty}_{pc,gc}$	$= 0.33 \times q^{\infty}_{pc,ent}$	h^{-1}		
$K_{pc,gc}[z]$	$= K_{pc,ent}[z]$	μm		
$\ell_{pc,gc}[z]$	$= \ell_{pc,ent}[z]$	μm		
$K_{pc,gc}[but]$	$K_{pc,ent}[but]$			
$\ell_{pc,gc}[but]$	$\ell_{pc,ent}[but]$			
$q^{\infty}_{ex,gc}$	0.34	h^{-1}		
$K_{ex,gc}[z]$	190	μm		
$\ell_{ex,gc}[z]$	15	μm		
$K_{ex,gc}[dens]$	20	$cell$		
$\ell_{ex,gc}[dens]$	$\ell_{div,}[dens]$	$cell$		
$q^{\infty}_{ex,ent}$	$= q^{\infty}_{ex,gc}$	h^{-1}		
$K_{ex,ent}[z]$	$K_{ex,gc}[z]$	μm		
$\ell_{ex,ent}[z]$	$\ell_{ex,gc}[z]$	μm		
$K_{ex,ent}[dens]$	$= K_{ex,gc}[dens]$	$cell$		
$\ell_{ex,ent}[dens]$	$= \ell_{ex,gc}[dens]$	$cell$		
s_o	-4	$\emptyset$	Stoechiometric coefficient for O_2	-
s_b	-1	$\emptyset$	Stoechiometric coefficient for butyrate	-
σ_o	3.6×10^6	$\mu m^2/h$	Diffusion coefficient for O_2	[42]
σ_{but}	$= \sigma_o$	$\mu m^2/h$	Diffusion coefficient for butyrate	-
γ^{∞}_{β}	1.6×10^4	$10^-15 \times \frac{mmol}{h \times \mu m^2}$	Max. reaction speed of β-oxydation	[18]
K_{β}	$(0.184 \times 10^4)^{1/5}$	mM	Affinity of β-oxydation	[19]
$c_{b,lum}$	5	mM	Luminal concentration of butyrate at homeostasis	[32]
$c_{o,bot}$	10	a.u.	Homestatic O_2 concentration at the bottom of the crypt	[54]

Parameter	Value
W	6.01/8
D	12.03
γ_β^∞	$1.6 \times 10^4/15.5$
ρ_{sc}^{bot}	0.65
ρ_{pc}^{bot}	0
ρ_{mc}^{bot}	0
ρ_{ent}^{bot}	0
z_d	3
d	2.25
z_u	3
u	-1/8

Table 12: Parameters used for numerical explorations of the deterministic approximation